Vaasan yliopisto
UNIVERSITY OF VAASA

.

Abrham Yitagesu Weldeyes

Thermo-Economic and Exergetic Optimization of a Sub-critical Organic Rankine Cycle for Micro Gas Turbine Exhaust Heat Recovery

School of Technology and Innovations
Major of Electrical Engineering
Master's Programme in Electrical and Energy Engineering

Vaasa 2026

UNIVERSITY OF VAASA
School of Technology and Innovations
Author: Abrham Yitagesu Weldeyes
Title of the thesis: Thermo-Economic and Exergetic Optimization of a Sub-critical Organic Rankine Cycle for Micro Gas Turbine Exhaust Heat Recovery
Degree: Master of Science in Technology
Degree Programme: Master's Programme in Electrical and Energy Engineering
Supervisor: Professor, Ward DE PAEPE, University of Mons.
Year: 2026 **Pages:** 73

ABSTRACT:

Micro gas turbines (mGTs) are used in distributed generation and combined heat and power systems, but their post-recuperator exhaust often leaves at 200–300 °C and is released without further use. This remaining heat can be recovered with a subcritical Organic Rankine Cycle (ORC) to produce additional electricity. However, the design is not straightforward because net power output, exergy destruction, and specific investment cost cannot all be improved at the same time. This thesis aims to identify the best-compromise ORC design for a 240 °C mGT exhaust stream using a three-objective NSGA-II optimisation framework. The ORC model was built for steady-state operation. It calculates the cycle performance and represents the heat recovery unit with separate preheater and evaporator zones. It also includes gas-side pressure-drop losses, exergy destruction, and purchased equipment cost. For each feasible design, it gives Pnet, TED, and SIC. NSGA-II is used to optimise these objectives through seven decision variables, including operating pressures, working-fluid mass flow rate, and heat-exchanger geometry. Four hydrocarbon fluids are analysed n-pentane, cyclopentane, n-hexane, and n-heptane. The final Pareto solutions are then ranked using TOPSIS. n-Pentane is selected as the best-compromise fluid. It gives a Pnet of 15.96 kW, an SIC of €7,169/kW, and an estimated simple payback of about 2.7 years at 8,000 h/yr under Belgian household electricity tariffs. Cyclopentane is the preferred alternative when minimising TED is more important, giving 22 % lower TED at 87 % of n-pentane's Pnet. Overall, n-pentane is the stronger choice when cost and power are the main priorities, while cyclopentane is better when thermodynamic quality is prioritised.

KEYWORDS: Organic Rankine Cycle, micro gas turbine, waste heat recovery, NSGA-II, TOPSIS, finned-tube heat exchanger, exergy destruction, specific investment cost

Table of Contents

Nomenclature

Symbol	Description	Unit
CAPEX	Capital expenditure (purchased-equipment cost)	€
C_e	Electricity retail tariff	€/kWh
CCi	TOPSIS closeness coefficient of solution i	–
c_p	Specific heat capacity	J/(kg·K)
d_c	Collar diameter	m
d_i / d_o	Tube inner / outer diameter	m
Ed	Exergy destruction rate in component	W
EF_{grid}	Grid electricity emission factor	kg CO_2e/kWh
f	Fanning friction factor	–
F	Convective enhancement factor	–
h	Specific enthalpy	J/kg
h_g	Gas-side convective heat-transfer coefficient	W/(m²·K)
h_{tp}	Two-phase boiling heat-transfer coefficient	W/(m²·K)
j	Colburn j-factor (gas-side heat transfer)	–
K_1, K_2, K_3	Turton cost correlation coefficients	–
m	Fin efficiency parameter	m^{-1}
M	Molecular mass of working fluid	kg/kmol
$\dot{m}_o$	ORC working-fluid mass flow rate	kg/s
$\dot{m}_g$	Exhaust-gas mass flow rate	kg/s
N_r	Number of tube rows	–
N_p	Number of parallel tubes per row	–
NTU	Number of transfer units	–
p	Fin pitch	m
Pc	Condensation pressure	Pa
P_{crit}	Critical pressure of working fluid	Pa
Pe	Evaporation pressure	Pa
P_f	Condenser fan power	W

P_{loss}	Gas-side auxiliary back-pressure power loss	W
Pnet	Net electrical power output	W
P_p	Pump shaft power	W
P_t	Turbine electrical power output	W
q	Local wall heat flux	W/m²
Q̇eva	Evaporator heat duty	W
Q̇pre	Preheater heat duty	W
S	Transverse tube spacing	m
SIC	Specific investment cost	€/kW
TC	Total purchased-equipment cost	€
TED	Total exergy destruction (all ORC components)	W
t	Fin thickness	m
U	Overall heat-transfer coefficient	W/(m²·K)
x	Vapor quality	–

Acknowledgements

I would like to express my sincere gratitude to my main academic supervisor, Professor Ward DE PAEPE, for his guidance, support, and valuable feedback throughout this thesis. His expertise and constructive advice helped me refine the research direction, improve the modelling approach, and strengthen the quality of this work.

I gratefully acknowledge the European Commission and the Erasmus+ Programme for awarding me the Erasmus Mundus scholarship, which made it possible for me to pursue the Joint Master on Smart Cities and Communities (SMACCs). I am also thankful to the SMACCs consortium and the partner universities for providing a rich academic and multicultural learning environment.

I would like to thank my professors, classmates, and friends for their encouragement, discussions, and support during the master's programme and thesis preparation.

Finally, I express my deepest appreciation to my family for their unconditional love, patience, sacrifices, and continuous encouragement. Their belief in me has been a constant source of strength throughout my studies.

Use of Artificial Intelligence

During the preparation of this thesis, the author used Grammarly AI tools to improve grammar, clarity, and language quality. In addition, AI-assisted tools were used to support the generation and refinement of programming code after the mathematical model had been developed by the author. The author takes full responsibility for the content of the thesis and confirms that the mathematical modelling, analysis, interpretation of results, and conclusions were developed and validated by the author.

List of Figures

List of Tables

1 Introduction

Micro gas turbines (mGTs) are small power units, typically in the range of 30 to 200 kW. They operate on the Brayton cycle and are used in distribution generation, combining heat and power (CHP), and remote power applications. Their small size, low maintenance needs, and fuel flexibility make them a good option for small-scale energy systems (Nami et al., 2018). However, even with a recuperator preheating the combustion air, a significant part of the fuel energy still leaves the system with exhaust gas. In recuperated mGTs, this exhaust usually exits the recuperator at around 200–300 °C and is often released to the atmosphere, even though it still has useful thermal and economic value (Papapetrou et al., 2018; Tudoroiu-Lakavice & Milusheva, 2023).

This temperature range is relevant in the wider European waste-heat context. Papapetrou et al. (2018) reported that about 70 % of European industrial waste heat is available below 300 °C. Therefore, mGT exhaust is located in the upper part of this low to medium temperature range. As shown in Figure 1, the 200–300 °C band is important for several European industrial sectors, including food processing, paper, and chemicals.

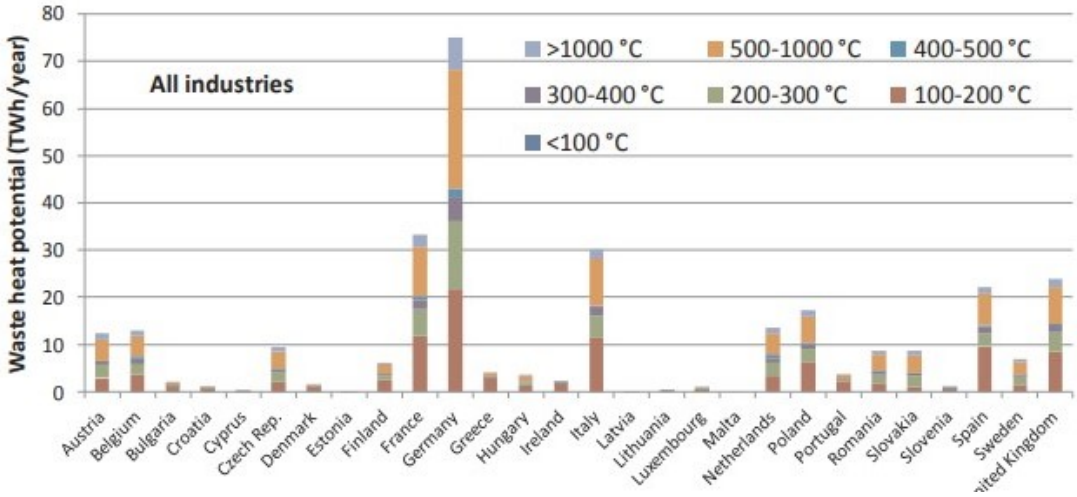

Figure 1.1: EU industrial waste-heat potential by temperature band across member states. The 200–300 °C range includes mGT exhaust and represents a relevant medium-temperature recovery opportunity (Tudoroiu-Lakavice & Milusheva, 2023).

1.1 mGT Exhaust Heat Recovery and Technology

The common ways to recover useful energy from mGT exhaust can be categorized into heating applications and ORC-based electricity generation. Heating applications use the

exhaust heat directly for heating by sending it to a district heating (DH) network to supply local heat demand. ORC-based recovery turns the exhaust heat into electricity, which can be used on site, sent to the grid, or stored.

District heating depends strongly on local heat demand. Cornelis and Van Bael (2016) showed that heat demand in summer is much lower than in winter in temperate European climates, which reduces the yearly use of an mGT connected to a DH network. Connolly et al. (2014) also noted that high DH penetration requires dense pipe infrastructure, which is often not available at small-scale mGT sites.

ORC electricity generation avoids this seasonal mismatch. The electricity produced is not directly limited by local heating demand, and Tartère and Astolfi (2017) reported that electricity-mode ORC plants typically achieve 6,000–8,000 full-load hours per year. In this work, the baseline heat source is a standalone recuperated mGT exhaust stream at 240 °C and 0.9 kg/s, with no specific heat consumer assumed. For this reason, pure electricity generation using an ORC is considered the most suitable recovery option for this work.

The ORC is a well-established technology for converting low and medium-temperature waste heat into electricity on a small scale. Quoilin et al. (2013) reviewed 73 installed waste-heat ORC plants and found specific investment costs of 1,500–4,500 €/kW, rising for units below 100 kW. Lecompte et al. (2015) concluded that the basic subcritical ORC is a practical choice for source temperatures below 350 °C, which fits the 240 °C mGT exhaust. Tartère and Astolfi (2017) documented over 700 installed ORC units, confirming the technology is commercially mature from small to large scales. At the 10–100 kW scale, the main components are the turbine-generator, boiler, condenser, and pump. Working-fluid selection determines cycle pressures, turbine design, and heat-exchanger sizing.

The ORC is preferred over other heat-to-power options for three reasons. First, thermoelectric generators have low efficiency at this temperature level and are not economically attractive on a large scale. Stirling engines can reach higher efficiencies but require precise components and regular maintenance, which is not suitable for remote or semi-attended mGT operation. The ORC uses mature turbomachinery and heat-exchanger components and can be matched to the exhaust temperature through working-fluid selection. Second, it scales to the 10–100 kW range without new technology development.

Third, its commercial track record provides a realistic basis for the cost assumptions used in this work.

1.2 Research Problem

Selecting and optimizing a compact subcritical ORC for mGT exhaust recovery is not straightforward, because the working fluid, heat-exchanger design, and system-level objectives are all closely linked.

First, there is no single best working fluid. Organic fluids differ in critical temperature, condensation pressure, latent heat, safety, and environmental impact. A fluid with a critical temperature near 240 °C can improve thermal matching and reduce boiler irreversibility (Nami et al., 2018), but may require sub-atmospheric condensation, increasing sealing complexity and cost. The Montreal Protocol and EU F-gas policy further restrict fluids with high ozone depletion or global warming potential. The fluid must therefore be selected by considering thermodynamic performance, pressure practicality, environmental rules, and cost together.

Second, the heat exchanger strongly affects both performance and economics. Nami et al. (2018) showed the evaporator is the dominant source of exergy destruction in gas-turbine exhaust ORC systems, and Yang et al. (2015) demonstrated that the preheater and evaporator must be modelled separately because their heat-transfer mechanisms differ significantly. At mGT scale, a larger heat-transfer area improves heat recovery but raises cost (Quoilin et al., 2013). Fin pitch, tube spacing, tube count, and row number must therefore be treated as design variables.

Third, the performance indicators conflict. Maximizing net power output (Pnet) favors larger exchangers and higher mass flow rates. Minimizing specific investment cost (SIC) favors compact designs. Minimizing total exergy destruction (TED) favors smaller temperature differences, which in turn raise costs. Because of these conflicts there is no single optimum point but rather there is a set of trade-off solutions.

This thesis therefore treats the problem as a three-objective optimization problem. The objectives are to maximize Pnet, minimize TED, and minimize SIC over seven decision variables which are evaporation pressure, condensation pressure, working-fluid mass flow rate, fin pitch, tube spacing, tube count, and row number. NSGA-II is applied per working fluid and TOPSIS is used to select the best-compromise design. The scope co-

vers steady-state design-point modelling for a fixed exhaust stream at 240 °C and 0.9 kg/s. The mGT itself is not modelled in detail, meaning the combustion process inside the mGT combustor, part-load operation, and dynamic control are all outside the scope of this work. Six candidate fluids are screened based on thermodynamic compatibility, environmental acceptability, and practical condensation pressure.

1.3 Aim and Objectives

The aim of this thesis is to identify the best-compromise subcritical ORC design for mGT exhaust heat recovery at 240 °C using a validated forward model, three-objective NSGA-II optimization, and TOPSIS decision-making.

The specific objectives are:

- Develop a steady-state ORC model combining thermodynamic cycle analysis, two-zone finned-tube heat-exchanger sizing, exergy accounting, and equipment cost estimation.
- Screen six candidate working fluids based on thermodynamic compatibility, environmental compliance, and condensation-pressure practicality.
- Apply NSGA-II to each fluid using three objectives
- Apply weighted TOPSIS to select the best-compromise design and recommend the working fluid.

1.4 Thesis Structure

Chapter 2 reviews the relevant literature and identifies the research gap. Chapter 3 develops the ORC model, covering the thermodynamic cycle, two-zone heat exchanger, pressure-drop calculation, exergy analysis, cost estimation, and model validation. Chapter 4 presents the NSGA-II optimization method and the TOPSIS decision-making framework. Chapter 5 presents the fluid screening, sensitivity analysis, Pareto results, selected design assessment, and Belgian case economic and environmental evaluation. Chapter 6 gives the main conclusions, limitations, and recommendations for future work.

2 Literature Review

This chapter reviews literature in five areas that are used to build the modelling and optimization framework of this study. These include ORC systems for exhaust heat recovery, working-fluid selection, finned-tube heat-exchanger design, exergy and thermo-economic indicators, and multi-objective optimization. The chapter closes by identifying the specific research gap the present study addresses.

2.1 ORC Systems for Exhaust Heat Recovery

Tchanche et al. (2011) surveyed ORC uses across several heat-source types of waste heat, solar, geothermal, and biomass and found that exhaust recovery from engines and gas turbines is one of the most active application areas. This is mainly because industrial and transport exhaust streams still contain a large amount of unused thermal energy. They also noted that a working fluid chosen for a low-temperature geothermal application may not be suitable for engine or gas-turbine exhaust, because the temperature range is different and the fluid properties must match the heat source.

Lecompte et al. (2015) compared five ORC cycle configurations and found that the basic subcritical cycle gives a reasonable balance between cost and performance when the heat source is below 350 °C. This range covers the mGT exhaust temperature used in the present work. Sprouse and Depcik (2013) focused on engine-exhaust ORCs and showed that the gas-to-liquid heat exchanger is one of the main design challenges. Exhaust gas transfers heat poorly compared to liquids, so the heat exchanger needs a large gas-side surface area to recover enough energy. However, a large surface area also increases gas-side pressure drop, and that pressure drop directly reduces the net power output by increasing blower work.

Nami et al. (2018) carried out exergy analysis on gas-turbine exhaust ORC systems and found that no matter which working fluid or cycle layout they used, the evaporator consistently accounted for the largest portion of exergy destruction. Yang et al. (2015) extended this to a diesel-engine exhaust case and modelled the preheater and evaporator as two separate zones rather than one combined boiler. This is important because single-phase liquid heating in the preheater has a much lower heat-transfer coefficient than boiling in the evaporator. In their results, the preheater alone accounted for up to 80 %

of the total heat-transfer surface. Treating the two zones as one boiler led to inaccurate estimates for both the required area and where the exergy losses were occurring.

Taken together, these studies show that the heat exchanger cannot be treated as a background component in ORC design. Both the thermal performance and the exergy losses of the system are strongly shaped by how the heat exchanger is modelled and sized. For mGT exhaust recovery, where the gas-side conditions are fixed and the working fluid is the main design variable, accurate heat-exchanger modelling is essential. For this reason, the present work uses a separate two-zone model for the preheater and evaporator rather than a single lumped boiler.

2.2 Working-Fluid Selection

Choosing a working fluid for an ORC is one of the main challenges in the design process. There is no universal best choice. The fluid needs to perform well thermodynamically, but it also must work safely, fit within pressure limits, and comply with environmental regulations. The main criteria reported in the literature are thermal efficiency, net power output, operating pressures, latent heat, heat-transfer behavior, toxicity, flammability, ODP, and GWP. No fluid satisfies all these criteria simultaneously.

Bao and Zhao (2013) gave a widely used classification. They split organic fluids into dry, isentropic, and wet types based on the slope of the saturated-vapor line in the T–s diagram. Dry and isentropic fluids are generally preferred in ORC turbines because the vapor stays superheated or just saturated at the end of expansion, which avoids liquid droplets and the blade erosion that comes with them. They also reviewed zeotropic mixtures, which can reduce exergy destruction in the boiler by matching the temperature glide of the mixture to the heat-source cooling curve. However, the mixture composition becomes another variable that must be optimized. Their classification is a useful starting point for fluid screening, but they noted that pressure limits, stability, safety, and heat-exchanger compatibility also need to be checked.

Saleh et al. (2007) screened 31 organic fluids using the BACKONE equation of state and applied pinch analysis to check feasibility. Their main finding was that the fluid giving the highest cycle thermal efficiency is not the same as the fluid that recovers the most heat from the source. High-boiling dry fluids like pentane and hexane isomers can give good thermal efficiency, but the pinch constraint often forces a large temperature gap

between the exhaust and the working fluid, which reduces the fraction of exhaust heat recovered in the heat exchanger. For waste-heat recovery applications, this is important because the aim is to recover as much useful exhaust energy as possible.

Tchanche et al. (2009) studied 20 fluids for a low-temperature solar ORC using a combined set of thermodynamic, safety, and environmental criteria. R134a ranked highest on thermodynamic grounds, but n-butane and isobutane were close behind, with the flammability issue as the main drawback. Wang et al. (2011) did something similar for engine exhaust recovery and found that older refrigerants like R11, R141b, and R123 performed slightly better thermodynamically, but R245fa and R245ca became more suitable once ODP and GWP limits were applied.

The pattern across all these screening studies is quite consistent. Fluid rankings change significantly when environmental and safety constraints are added. A fluid that looks like a strong candidate based on thermal efficiency alone can drop out of consideration when factors in GWP limits or flammability are considered. This means fluid screening cannot be done in two separate steps thermodynamic first, then environmentally. Both need to be considered together from the start, which is the approach taken in the present work.

Regulations have also changed which fluids are practical for use. The Montreal Protocol (UNEP, 2018) phased out many of the older high-ODP refrigerants, and EU F-gas restrictions have since pushed further toward fluids with low GWP. These rules have narrowed the field of practical ORC working fluids considerably. The alternatives that remain fall into three main groups. Hydrocarbons such as pentane, butane, and their isomers have zero ODP and very low GWP, which makes them environmentally favorable, but their flammability means that system design and installation need to account for safety requirements. HFOs are another option, with low ODP and low GWP, but they have less operational history in ORC systems compared to the older refrigerants, so some uncertainty remains about long-term performance. Zeotropic mixtures offer more flexibility because the temperature glide can be tuned to match the heat source better, but this comes with added complexity in selecting the right composition and in controlling the system over time (Bahrami et al., 2022). In practice, none of these groups is clearly superior. The right choice depends on the specific heat-source temperature, the safety setup at the installation site, and the regulatory environment.

2.2.1 Exergy Efficiency as a Fluid Selection Indicator

One issue in working-fluid comparisons is that thermal efficiency is not always the most informative metric. Elahi et al. (2022) showed this when comparing fluids with different critical temperatures and pressure levels, thermal efficiency can give a misleading picture because it only looks at how much of the heat input is converted to work, without considering the quality of that heat.

Exergy efficiency addresses this differently. It compares the actual net power output not to the heat input, but to the maximum theoretical work that could be obtained from the heat source at its given temperature. A heat source at 240 °C has more useful work potential, more exergy than a source at 100 °C carrying the same amount of energy. If a working fluid operates at pressures and temperatures that are not well matched to the 240 °C source, a large part of that work potential is destroyed in the heat exchanger, even if the cycle appears efficient by thermal efficiency standards.

In practice this means two fluids can have similar thermal efficiencies but quite different exergy efficiencies if one fits the exhaust temperature profile better than the other. A fluid that achieves high thermal efficiency by working at high condensation pressure and small pressure ratio may still destroy more exergy in the boiler than a fluid that matches the temperature profile more closely at a lower cycle efficiency. Elahi et al. (2022) confirmed this in their multi-fluid comparison, which is why exergy performance is considered in the present work by using total exergy destruction as one of the optimization objectives, together with net power and specific investment cost rather than relying on thermal efficiency alone.

2.3 Finned-Tube Evaporator and Preheater Design

The heat-exchanger model used in this thesis follows the two-zone approach introduced by Yang et al. (2015), who separated the heat-addition section into a preheater zone and an evaporator zone. In the preheater, the compressed liquid is heated up to the saturation temperature. In the evaporator, the fluid undergoes phase change at roughly constant temperature. These two zones have quite different heat-transfer characteristics, so they need different correlations. Yang et al. (2015) used a j-factor correlation for the gas-side convection over staggered plate-fin tube banks, the Gnielinski correlation for single-

phase flow inside the tubes, and the Liu–Winterton superposition model for two-phase boiling. These correlations provide the basis for the heat-exchanger modelling approach used in the present work.

Maalouf et al. (2012) studied how individual geometric parameters affect the overall performance of a finned-tube ORC evaporator. They found that fin pitch, tube diameter, gas-side velocity, and tube-side mass velocity cannot be changed independently by adjusting one of them shifts the compactness, the gas-side pressure drops, and the exergy losses all at the same time. For a flue-gas inlet of 110 °C, their best design had a fin pitch around 3 mm, and wavy fins gave a more compact exchanger than plain fins without increasing the pressure drop. Their main conclusion is that heat-exchanger geometry needs to be treated as a design variable, not a fixed input.

Zhang et al. (2021) confirmed this using CFD optimization on a fin-and-tube evaporator. They reported meaningful improvements in the area goodness factor and friction characteristics by changing tube and fin geometry, although CFD is too expensive to run inside a full ORC system optimization loop. For the present work, geometry parameters such as fin pitch, tube spacing, tube count, and row number are included as decision variables in the optimization, which is consistent with the direction suggested by all three studies.

2.4 Exergy and Thermo-Economic Indicators

Standard energy analysis gives net power, heat input, and cycle efficiency, but it does not indicate where useful work potential is irreversibly lost. In ORC design this matters because components like the evaporator can look fine from an energy balance perspective while destroying a large fraction of the available exergy. Nami et al. (2018) showed this clearly for gas-turbine exhaust systems the evaporator was the largest source of exergy destruction in every case they studied. Yang et al. (2015) took the next step and used exergy destruction rate not just as a diagnostic metric but as a direct optimization objective. This means the design process aims to reduce irreversibility, rather than only measuring it afterwards.

On cost, Quoilin et al. (2013) pointed out that below 100 kW, ORC specific investment cost is very sensitive to component choices. Custom heat exchangers and expanders can account for most of the system cost at this scale, so small changes in geometry or

working fluid can have a large effect on the overall price. Hettiarachchi et al. (2007) used heat-transfer area per unit net power as a cost proxy, which works reasonably well when heat-exchanger cost scales with area. Imran et al. (2014) optimized thermal efficiency and specific investment cost at the same time using NSGA-II and found that a regenerative ORC configuration improved thermal efficiency by about 1 % but increased specific investment cost by around 190 USD/kW. That trade-off is not visible when only one objective is optimized.

This indicates there is a broader issue with single-objective optimization in ORC design. Net power, exergy destruction, and specific investment cost influence the design in different ways. A design that maximizes net power tends to use large heat exchangers and high working-fluid flow rates, which drives up cost. A design that minimizes cost tends to use compact heat exchangers, which increases exergy destruction and reduces power. A design that minimizes exergy destruction tends to use small temperature differences across the heat exchanger, which again requires more area and higher cost. There is no single design that is best on all three at once. A suitable way to understand these trade-offs is to treat all three as simultaneous objectives and examine the full Pareto front, which is the approach adopted in this work.

2.5 Multi-Objective Optimization in ORC Studies

Because of ORC performance objectives conflict, single-objective optimization will always produce a design that has been over-optimized for one aspect at the expense of the others. Pareto-based methods avoid this by finding all non-dominated solutions at once, giving the designer a complete picture of the available trade-offs rather than just one point on that surface.

Hu et al. (2021) reviewed 122 multi-objective ORC optimization studies and found that roughly 75 % used only two objectives, and just 16 % used three. NSGA-II appeared in 66 % of all the studies, making it by far the most commonly used algorithm. Hu et al. (2021) also noted that most studies only varied system-level variables like evaporation and condensation pressure. Few studies included component-level geometry such as heat-exchanger fin or tube parameters or working-fluid identity in the same optimization problem. This integration of multiple design levels is still relatively uncommon, and it is one contribution of the present work.

NSGA-II, developed by Deb et al. (2002), sorts the population into non-domination levels, preserving the best solutions across generations through elitist selection, and maintaining diversity using crowding distance which does not need any user-defined sharing parameters. Imran et al. (2014) and Wang et al. (2013) both used NSGA-II for ORC thermo-economic optimization and confirmed it handles conflicting objectives well in practice.

Once a Pareto front is obtained, a decision-making method is needed to select one design. Behzadian et al. (2012) reviewed TOPSIS across 266 published applications, ranks alternatives by how close they are to the ideal solution and how far they are from the anti-ideal solution. It is straightforward to apply, can be applied directly to the objective values without needing assumptions about the shape of the Pareto front, and the final ranking can be adjusted by changing the weights assigned to each objective.

2.6 Research Gap

The reviewed literature establishes that ORC systems are well suited to medium-temperature exhaust heat recovery (Tchanche et al., 2011; Lecompte et al., 2015; Sprouse & Depcik, 2013); that working-fluid selection requires balancing thermodynamic, environmental, safety, and pressure constraints (Bao & Zhao, 2013; Saleh et al., 2007; Elahi et al., 2022; UNEP, 2018; Tchanche et al., 2009; Wang et al., 2011; Bahrami et al., 2022); that separated two-zone finned-tube heat-exchanger models with geometric variables substantially improve design accuracy compared to lumped models (Yang et al., 2015; Maalouf et al., 2012; Zhang et al., 2021); that net power, exergy destruction, and specific investment cost capture complementary and partially conflicting performance aspects (Quoilin et al., 2013; Nami et al., 2018; Elahi et al., 2022; Hettiarachchi et al., 2007; Imran et al., 2014); and that NSGA-II with TOPSIS is an established and validated approach for multi-objective ORC optimization (Behzadian et al., 2012; Imran et al., 2014; Wang et al., 2013).

No reviewed study fully addresses the present mGT exhaust recovery problem. Imran et al. (2014) and Wang et al. (2013) used lumped heat-exchanger models and omitted exergy destruction; Yang et al. (2015) used a two-zone model with exergy objectives but covered a single refrigerant and excluded SIC; Hu et al. (2021) confirmed that three-objective combined thermo-economic–energetic optimization with geometric decision

variables remains uncommon. Within the reviewed literature, no study simultaneously combines a 240 °C mGT exhaust source, three objectives (Pnet, TED, SIC), a two-zone finned-tube model with geometric variables, and Pareto comparison across multiple hydrocarbon working fluids. The present work addresses this gap.

3 ORC Model Development

This chapter presents the ORC model used in multi-objective optimization. It covers the physical system, thermodynamic cycle calculations, two-zone finned-tube heat-exchanger model, gas-side pressure-drop terms, exergy accounting, equipment cost model, and feasibility constraints. For each feasible design, the model calculates three outputs: net electrical output Pnet, total exergy destruction TED, and specific investment cost SIC. These are the three objectives used by NSGA-II. The seven decision variables are evaporation pressure Pe, condensation pressure Pc, working-fluid mass flow rate $\dot{m}_o$, fin pitch p, tube spacing S, number of parallel tubes per row N_p, and number of tube rows N_r. Figure 3.1 shows the calculation sequence used in the model. The chapter also explains the validation procedure based on Yang et al. (2015), using the same main heat-exchanger correlations. Full geometry expressions, correlation coefficients, and cost data are in Appendix A.

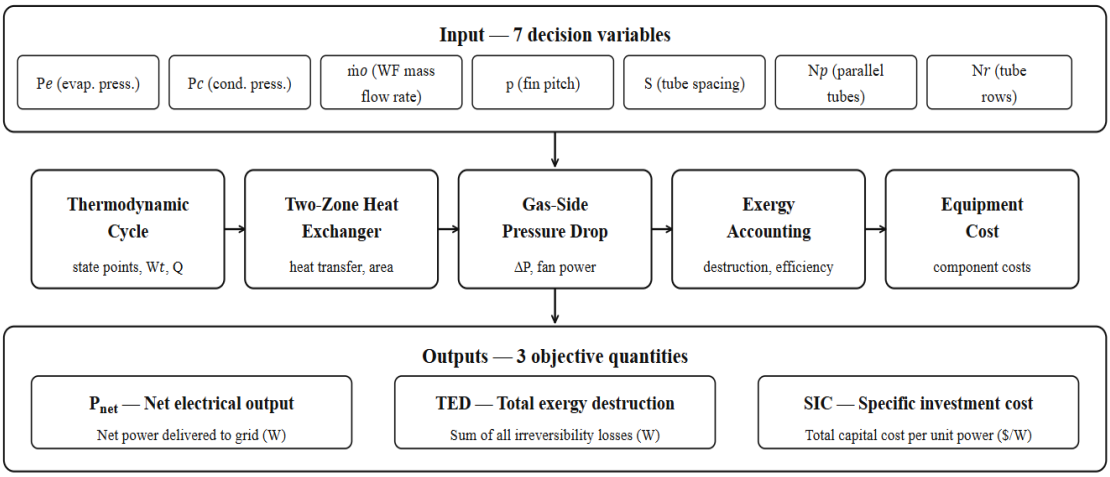

Figure 3.1: Sequential modelling framework of the ORC model. The seven decision variables pass through the thermodynamic, heat-exchanger, pressure-drop, exergy, and cost sub-models to return Pnet, TED, and SIC.

3.1 Model Scope and Main Assumptions

The ORC model is developed for steady-state, steady-flow conditions. This approach is common for preliminary ORC sizing and design comparison (Quoilin et al., 2013; Lecompte et al., 2015). Connecting pipework is assumed to be adiabatic, and heat losses from component surfaces are neglected. Enthalpy changes are therefore only calculated

for the main ORC components. The model is vali-dated with a published ORC result in Section 3.10. The numerical results of this check are reported in Chapter 5.

The heat-addition section is split into sensible preheater and a saturated evaporator, rather than being treated as a single lumped boiler. In the preheater, the organic fluid is compressed liquid heated from the pump outlet to the saturated-liquid state at Pe. In the evaporator, it boils at nearly constant saturation temperature. Yang et al. (2015) showed that combining these two zones into one averaged heat-transfer coefficient leads to significant errors in area estimation. The two-zone approach also allows the pinch-point location and the preheater gas outlet temperature to be calculated separately, which is needed for the acid dew-point check. The mGT itself is not modelled in detail. It is treated as a fixed exhaust source with known temperature, pressure, and mass flow rate.

3.2 System Configuration and Boundary Conditions

The ORC system is represented as a basic subcritical cycle connected to the post-recuperator exhaust of a recuperated micro gas turbine, as shown in Figure 3.2. The working fluid leaves the condenser as saturated liquid at State 1, is compressed from Pc to Pe by the pump, and enters the heat-addition section at State 2. Heat addition is split into two zones: the preheater raises the compressed liquid to saturated liquid at State 2', and the evaporator provides the latent heat to reach saturated vapor at State 3. The vapor then expands through the turbine to Pc, giving the actual outlet State 4. The condenser rejects the remaining heat and returns the fluid to State 1.

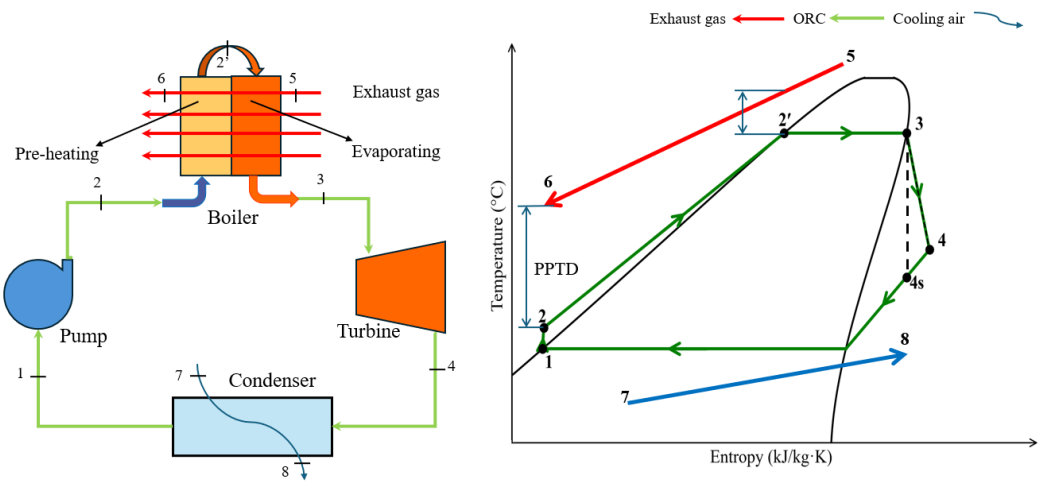

Figure 3.2 Schematic of the subcritical ORC and corresponding T–s diagram.

A basic subcritical cycle is chosen rather than a supercritical layout. Lecompte et al. (2015) showed that the subcritical cycle gives the best cost-to-performance balance for heat sources below 350 °C, which includes the 240 °C mGT exhaust used here. For a small-scale waste-heat recovery system at this temperature level, the subcritical layout is the more practical choice.

The turbine inlet is fixed at saturated vapor with no superheating. For dry and isentropic fluids, this avoids unnecessary boiler area while keeping vapor-phase expansion throughout the turbine (Saleh et al., 2007). State 1 is defined by saturated-liquid properties at Pc, State 2′ by saturated-liquid properties at Pe, and State 3 by saturated-vapor properties at Pe. Organic-fluid properties are calculated using CoolProp (Bell et al., 2014). Exhaust-gas properties are calculated from the temperature-dependent correlations in Appendix A.

The exhaust stream is set to a design-point condition of 240 °C, 1.05×10^5 Pa, and 0.9 kg/s. These values are used to represent the post-recuperator exhaust of a Turbec T100-class mGT. These values are based on experimental data provided for the 100 kW micro gas turbine dataset from the Thermal Engineering and Combustion Unit at UMONS. The average temperature and mass-flow values of the flue gas are 240 °C and 0.9 kg/s. The dead state is T_o = 284.15 K and P_o = 101 325 Pa. Component efficiencies are assumed with fixed values at η_t = 0.70 for the turbine, η_p = 0.70 for the pump, η_g = 0.98 for the generator, and η_{fan} = 0.80 for the condenser fan. These are conservative estimates for small-scale ORC performance (Quoilin et al., 2013).

The condensation temperature is kept at least 50 °C for air-cooled operation, and the preheater gas outlet must stay above 70 °C to avoid acid dew-point corrosion (Yang et al., 2015; Bahrami et al., 2022). The boiler tubes have fixed outer and inner diameters of 12.7 mm and 10.7 mm, and the fins are 0.3 mm thick, made of stainless steel. These tube and fin dimensions are fixed geometric inputs, not decision variables. The geometric decision variables are fin pitch p, tube spacing S, number of parallel tubes per row N_p, and number of tube rows N_r. These four variables are optimized for the exhaust-side heat-recovery section. The condenser geometry is not optimized. The condenser is modelled as a simplified air-cooled unit with a fixed overall heat-transfer coefficient, and a prescribed air-side pressure drop. This simplified condenser model is sufficient for estimating condenser duty, fan power, and cost, because the optimization focuses on the exhaust-side heat-recovery section rather than detailed condenser geometry. Equipment costs are taken from Turton et al. (2008) (2001 base year) and updated to 2024 using the CEPCI index.

3.3 Thermodynamic Cycle Model

The energy balances below are based on the state-point definitions and efficiency values given in Section 3.2.

3.3.1 Pump Model

The pump is modelled as an adiabatic component that compresses saturated liquid from Pc to Pe. The isentropic outlet enthalpy h_{2s} is found at Pe for constant entropy s_1. The actual pump power $\dot{w}_p$ is calculated using the pump isentropic efficiency η_p = 0.70 (Cooper, 1984):

$$h_{2s} = h(\mathrm{Pe}, s_1) \tag{3.1}$$

$$h_2 = h_1 + \frac{h_{2s} - h_1}{\eta_p} \tag{3.2}$$

$$P_p = \dot{m}_o(h_2 - h_1) \tag{3.3}$$

Because the pump outlet is subcooled liquid at Pe, heat addition starts with sensible preheating before boiling begins.

3.3.2 Turbine and Generator Model

The turbine receives saturated vapor at State 3 and expands it to Pc. The actual turbine outlet state is calculated using the turbine isentropic efficiency ηt = 0.70. The electrical power Pt is then found using the generator efficiency ηg = 0.98 (Yang et al., 2015; Cooper, 1984):

$$h_{4s} = h(\mathrm{Pc}, s_3) \tag{3.4}$$

$$h_4 = h_3 - \eta_t(h_3 - h_{4s}) \tag{3.5}$$

$$W_t = \dot{m}_o(h_3 - h_4) \tag{3.6}$$

$$P_t = \eta_g W_t \tag{3.7}$$

3.3.3 Condenser and Net-Power Model

The condenser removes the heat $\dot{Q}_c$ needed to return the turbine outlet vapor at State 4 to saturated liquid at State 1. Condenser fan power P_f and the gas-side auxiliary blower penalties $P_{loss,e}$ and $P_{loss,p}$ are all subtracted from the turbine electrical output to give net power (Nami et al., 2018; Yang et al., 2015):

$$Q_c = \dot{m}_o(h_4 - h_1) \tag{3.8}$$

$$P_f = \frac{\dot{m}_a}{\rho_a}\frac{\Delta P_{a,\mathrm{cond}}}{\eta_{\mathrm{fan}}} \tag{3.9}$$

$$\mathrm{P}net = P_t - P_p - P_f - P_{\mathrm{loss},e} - P_{\mathrm{loss},p} \tag{3.10}$$

The terms $P_{loss,e}$ and $P_{loss,p}$ are the hydraulic powers needed to move the exhaust gas through the evaporator and preheater against the gas-side pressure drop. They represent the back-pressure load on the mGT exhaust. Subtracting them in Eq. (3.10) means that adding rows or closing fin pitch to improve heat recovery can also reduce Pnet through higher backpressure. For this reason, heat-exchanger geometry is included in the optimization.

3.4 Heat-Duty Separation and Pinch-Point Logic

The total heat input is divided into an evaporation duty $\dot{Q}_e$ and a preheating duty $\dot{Q}_p$. Both are calculated from the working-fluid enthalpy change across each zone. The

exhaust-side energy balance uses a mean specific heat capacity from the correlations in Appendix A:

$$Q_e = \dot{m}_o(h_3 - h_{2,}) \tag{3.11}$$

$$Q_p = \dot{m}_o(h_{2,} - h_2) \tag{3.12}$$

$$Q_g = \dot{m}_g c_{p,g}\left(T_{g,\text{in}} - T_{g,\text{out}}\right) \tag{3.13}$$

The evaporator is solved first, from the hot exhaust inlet. The preheater uses the gas temperature leaving the evaporator as its inlet. This follows the physical exhaust flow direction and ensures the hottest gas is used where it has the highest thermodynamic value. The two-zone split also makes the pinch-point location visible. If the limiting temperature approach is near the cold end, the preheater length and gas outlet temperature control heat recovery. If it is inside the evaporation zone, the boiling temperature and exhaust inlet temperature are the main controlling variables (Yang et al., 2015).

3.5 Finned-Tube Heat-Exchanger Model

The heat exchanger is modelled by splitting the thermal resistances into three parts. Gas side, tube wall, and working-fluid side. Figure 3.3 shows the staggered finned-tube arrangement. The transverse tube spacing S, longitudinal spacing S_l, tube outer diameter d_o, fin pitch p, and fin thickness t together define the gas-flow geometry, external heat-transfer area, and pressure-drop path. Full geometry expressions are in Appendix A.

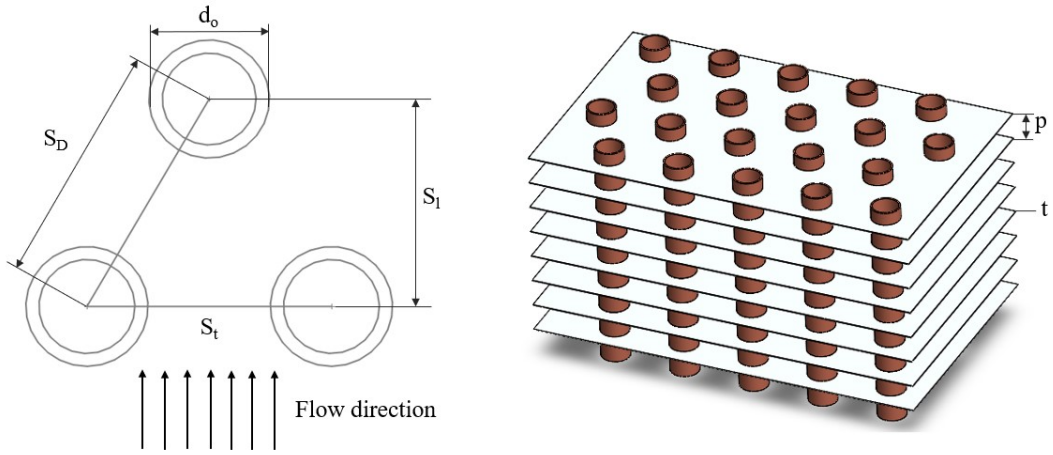

Figure 3.3: Staggered finned-tube heat-exchanger geometry used for the preheater and evaporator model.

The Reynolds, Prandtl, and Nusselt numbers are used for the exhaust side, the single-phase organic side, and the liquid-only term in the boiling correlation.

$$Re = \frac{\rho V L_c}{\mu} = \frac{G L_c}{\mu} \tag{3.14}$$

$$Pr = \frac{c_p \mu}{k} \tag{3.15}$$

$$h = \frac{Nu\, k}{L_c} \tag{3.16}$$

For internal tube flow, the characteristic length L_c is the tube inner diameter d_i. For the gas-side correlation, L_c is the collar diameter d_c.

3.5.1 Gas-Side Heat Transfer and Friction

The gas side dominates the overall thermal resistance because its heat-transfer coefficient is much lower than the liquid or boiling coefficient inside the tubes. The plain-fin correlation of Wang et al. (2000), based on experimental data for staggered tube banks, gives the Colburn *j* factor and Fanning friction factor *f* as functions of Reynolds number, fin pitch, tube spacing, and row count:

$$j = 0.086\, Re^{a_1} N_r^{a_2} \left(\frac{p}{d_c}\right)^{a_3} \left(\frac{p}{d_h}\right)^{a_4} \left(\frac{p}{S}\right)^{-0.93} \tag{3.17}$$

$$f = 0.0267\, Re^{b_1} \left(\frac{S}{S_l}\right)^{b_2} \left(\frac{p}{d_c}\right)^{b_3} \tag{3.18}$$

$$Nu_g = j\, Re_g\, Pr_g^{1/3} \tag{3.19}$$

The coefficient groups a_1–a_4 and b_1–b_3 are listed in Appendix A, Section A.3. The gas-side heat-transfer coefficient is then found from Eq. (3.19) using Eq. (3.16), with L_c equal to the collar diameter d_c. Since the evaporator is solved row by row, the mean gas-side coefficient is corrected by a row-weighting factor to account for how heat transfer changes through the tube bank (Chea and Elbel (2021); Halici et al. (2001)). These factors are in Appendix A, Section A.4. For $N_r \geq 5$ the factor levels off, so the correlation remains valid across all N_r values used in the optimization.

3.5.2 Fin Efficiency and Overall Heat Transfer Coefficient

The fin efficiency η_f for circular annular fins is found using the modified-Bessel-function expression given in Appendix A. This gives more accurate results than the simpler tanh approximation at the fin radius ratios used here (Hettiarachchi et al., 2007; Imran et al.,

2014). The Schmidt equivalent-radius method is used to convert the hexagonal fin arrangement to an equivalent annular geometry (Schmidt, 1949).

The overall surface efficiency η_o accounts for the mix of bare tube areas and finned areas on the gas side. It is defined as:

$$\eta_o = \frac{\left(A_{gbare} + \eta_f A_{gfin}\right)}{A_{gtotal}} \tag{3.20}$$

where A_{gfin} is the fin surface area and $A_{g,total}$ is the total gas-side area. The overall thermal resistance has three series terms gas-side convection over the bare and finned surfaces, tube-wall conduction, and working-fluid convection (Imran et al., 2014; Wang et al., 2000):

$$\frac{1}{U} = \frac{A_{g,\text{total}}}{h_o A_o} + \frac{A_{g,\text{total}} \ln(d_o/d_i)}{2\pi k_m L N_t} + \frac{1}{\eta_o h_g} \tag{3.21}$$

(Eq. (3.20) is applied in both preheater and evaporator. In the preheater, h_o is the single-phase liquid coefficient. In the evaporator, it is replaced by the local two-phase boiling coefficient h_{tp}.

3.5.3 Single-Phase Liquid Heat Transfer in the Preheater

For laminar flow (Re < 2300), the thermally developing Sieder–Tate expression is used because organic liquids can carry a significant bulk-to-wall viscosity gradient that the simpler Dittus–Boelter form ignores (Imran et al., 2014; Sieder & Tate, 1936):

$$Nu_{\text{lam}} = 1.86 \left(\frac{Re\, Pr\, d_i}{L}\right)^{1/3} \left(\frac{\mu}{\mu_w}\right)^{0.14} \tag{3.22}$$

For turbulent flow (Re > 3000), the Gnielinski correlation is used because it accounts for friction and gives reliable results across the Reynolds-number range typical for ORC fluids (Gnielinski, 1976):

$$f = (0.79 \ln Re - 1.64)^{-2} \tag{3.23}$$

$$Nu_{\text{turb}} = \frac{(f/8)(Re - 1000)Pr}{1 + 12.7(f/8)^{1/2}(Pr^{2/3} - 1)} \tag{3.24}$$

In the transition zone (2300 < Re < 3000), the Nusselt number is linearly interpolated between the laminar and turbulent values to avoid sudden jumps in the heat-transfer coefficient during optimization:

$$Nu = Nu_{\text{lam},2300} + \frac{Re - 2300}{700}\left(Nu_{\text{turb},3000} - Nu_{\text{lam},2300}\right) \tag{3.25}$$

3.5.4 Two-Phase Boiling Heat Transfer in the Evaporator

Boiling in the evaporator involves forced convective evaporation, which increases with vapor quality as the liquid film gets thinner, and nucleate boiling, which depends on local heat flux and reduced pressure. The Liu–Winterton correlation (Liu & Winterton, 1991) adds both contributions using a root-sum-square form. Yang et al. (2015) used the same correlation for a finned-tube ORC evaporator in engine exhaust recovery, which gives a direct connection to the model validation in Section 3.10. The evaporator is solved row by row. For each row, the average vapor quality is used to find the local two-phase coefficient h_{tp}:

$$h_{tp} = [(Fh_{cb})^2 + (S_b h_{nb})^2]^{1/2} \tag{3.26}$$

$$h_{cb} = 0.023\frac{k_l}{d_i}Re_l^{0.8}Pr_l^{0.4} \tag{3.27}$$

$$h_{nb} = 55\,P_r^{0.12}q^{2/3}[-\log_{10}(P_r)]^{-0.55}M^{-0.5} \tag{3.28}$$

$$F = \left[1 + \bar{x}Pr_l\left(\frac{\rho_l}{\rho_v} - 1\right)\right]^{0.35} \tag{3.29}$$

$$S_b = [1 + 0.055F^{0.1}Re_l^{0.16}]^{-1} \tag{3.30}$$

In Eq. (3.28), P_r is the reduced pressure Pe/P_{crit} and M is the molecular mass. The Cooper pool-boiling form is used because it does not need surface roughness data, which is not known at the design stage (Cooper, 1984). In Eq. (3.29), Pr_l is the liquid Prandtl number from Eq. (3.15). The local heat flux per row is:

$$q = \frac{Q_i}{\pi d_i L_i N_p} \quad [\mathrm{W/m^2}] \tag{3.31}$$

After each row, the solver updates the gas temperature, vapor quality, heat flux, fin efficiency, overall U, NTU, heat duty, and pressure drop before going to the next row.

3.5.5 NTU-Effectiveness and Iteration

The NTU-effectiveness method is used because it calculates the heat transfer in each zone without needing to fix the outlet temperatures first. This is useful during

optimization, where many candidate designs are tested (Wang et al., 2000; Turton et al., 2018). The number of transfer units is:

$$NTU = \frac{UA_{g,\text{total}}}{C_{\min}} \tag{3.32}$$

In the evaporator, the organic fluid evaporates at nearly constant temperature, so C_r approaches zero and the effectiveness simplifies to:

$$\varepsilon_e = 1 - \exp(-NTU) \tag{3.33}$$

$$Q_i = \varepsilon_e C_{\min}\left(T_{g,\text{in},i} - T_{\text{sat}}\right) \tag{3.34}$$

In the preheater, both streams change temperature. The NTU-effectiveness expression for this case is given in Appendix A. The tube length in each zone is found by bisection, adjusting the length until the NTU-calculated duty matches the enthalpy-based duty from Eqs. (3.11)– (3.12) within a relative error of 10^{-3}.

3.6 Pressure Drop and Auxiliary Losses

Any design with more rows or smaller fin pitch improves heat recovery but also increases gas-side flow resistance, creating a back-pressure load on the mGT exhaust. The associated auxiliary power P_{loss} is modelled as the hydraulic work needed to push the exhaust gas through the heat exchanger against the total gas-side pressure drop ΔP_g. It is the back-pressure penalty subtracted in Eq. (3.10), not a separately driven blower. Frictional and minor losses follow standard compact heat-exchanger expressions:

$$\Delta P_{\text{fric}} = \frac{G_g^2}{2\rho_g} f\left(\frac{A_{g,\text{total}}}{A_{g,\text{flow}}}\right) \tag{3.35}$$

$$\Delta P_{\text{minor}} = \frac{G_g^2}{2\rho_g}(K_c + K_e) \tag{3.36}$$

$$\Delta P_g = \Delta P_{\text{fric}} + \Delta P_{\text{minor}} \tag{3.37}$$

$$P_{\text{loss}} = \frac{\dot{m}_g}{\rho_g}\Delta P_g \tag{3.38}$$

Equations (3.35)–(3.38) are applied separately to the evaporator and preheater, giving $P_{loss,e}$ and $P_{loss,p}$, both of which appear in Eq. (3.10). The friction factor f is from Eq. (3.18); K_c and K_e are the entrance contraction and exit expansion coefficients (Kays and London (1998)).

3.7 Exergy Accounting

Energy analysis tracks heat and work transfers but does not show where useful work potential is lost. Exergy accounting is used here to identify where irreversibility occurs in the ORC components. TED is defined as the sum of internal component exergy destructions within the ORC boundary. Exhaust-stack exergy and discharged cooling-air exergy are treated as external losses and are not included in TED. The dead state is T_o = 284.15 K and P_o = 101 325 Pa.

The exergy of the exhaust is calculated using an ideal-gas approximation. At any exhaust-gas state k (Bahrami et al., 2022; Bejan et al. (1996)):

$$E_{xgk} = \dot{m}_g(c_{p,g}\left[(T - T_0) - T_0 \ln\left(\frac{T}{T_0}\right)\right] + R_g T_0 \ln\left(\frac{P}{P_0}\right)) \tag{3.39}$$

For any adiabatic heat exchanger with no work interaction, exergy destruction is calculated from entropy generation:

$$E_{d,\mathrm{HX}} = T_0(\dot{m}_{\mathrm{hot}}\Delta s_{\mathrm{hot}} + \dot{m}_{\mathrm{cold}}\Delta s_{\mathrm{cold}}) \tag{3.40}$$

Equation (3.40) is applied separately to the evaporator, preheater, and condenser. For the evaporator, the two streams are the exhaust gas and the organic fluid between States 2′ and 3. For the preheater, they are the exhaust gas and the organic fluid between States 2 and 2′. For the condenser, they are the organic fluid between States 4 and 1, and the cooling air between States 7 and 8.

$$E_{d,\mathrm{turb}} = \dot{m}_o[(h_3 - h_4) - T_0(s_3 - s_4)] - W_t \tag{3.41}$$

$$E_{d,pump} = P_p - \dot{m}_o[(h_2 - h_1) - T_0(s_2 - s_1)] \tag{3.42}$$

$$E_{d,\mathrm{gen}} = W_t - P_t \tag{3.43}$$

$$E_{d,\mathrm{fan}} = P_f - \dot{m}_a[\left(h_{f,out} - h_{f,in}\right) - T_0\left(s_{f,out} - s_{f,in}\right)] \tag{3.44}$$

$$TED = E_{d,\mathrm{evap}} + E_{d,\mathrm{pre}} + E_{d,\mathrm{turb}} + E_{d,\mathrm{gen}} + E_{d,\mathrm{cond}} + E_{d,\mathrm{fan}} + E_{d,\mathrm{pump}} \tag{3.45}$$

Equations (3.41)–(3.44) calculate the irreversibility in the turbine, pump, generator, and fan. Equation (3.45) adds to the heat-exchanger exergy destructions to give TED.

3.8 Thermo-Economic Cost Model

Equipment costs are estimated using Turton et al. log-quadratic correlations (Turton et al., 2008), a widely used method for preliminary equipment cost estimation. Heat

exchangers are scaled by total heat-transfer area, and the pump and turbine are scaled by power. The coefficients K_1, K_2, K_3, and the material factor Fm for stainless-steel construction are given in Appendix A.

$$\log_{10}\left(C_{p,2001}\right) = K_1 + K_2\log_{10}(X) + K_3[\log_{10}(X)]^2 \tag{3.46}$$

$$C_p = Fm\ C_{p,2001}\left(\frac{CEPCI_{2024}}{CEPCI_{2001}}\right) \tag{3.47}$$

$$\mathrm{T}C = C_{\mathrm{evap}} + C_{\mathrm{pre}} + C_{\mathrm{cond}} + C_{\mathrm{turb}} + C_{\mathrm{pump}} \tag{3.48}$$

$$SIC = \frac{\mathrm{T}C}{P_{\mathrm{net}}} \tag{3.49}$$

More heat-exchanger areas increase both equipment cost and heat recovery but also raises blower losses. This non-monotonic relationship between TC and Pnet is why SIC is included as an optimization objective rather than being calculated after the optimization.

3.9 Feasibility Constraints

Eight constraints are checked for each set of input variables. If any constraint fails, the model returns a penalty. The penalty values are given in Chapter 4.

- Pe > Pc positive turbine expansion pressure ratio.
- $0 < Pe/P_{crit} < 1$ strictly subcritical; boiling correlations are invalid above the critical point.
- p > t fin pitch must exceed fin thickness to form a physically open gas passage.
- $S > d_o + 1$ mm minimum tube clearance to prevent geometric overlap and gas-side blockage.
- $T_{sat}(Pc) \geq 50$ °C minimum condensation temperature, consistent with the condenser design basis.
- $T_{gp,out} \geq 70$ °C conservative acid dew-point safeguard for the preheater gas outlet (Yang et al., 2015).
- Pnet > 0 net electrical output must be positive after all parasitic deductions.
- $E_d \geq 0$ for all components negative exergy destruction violates the second law.

3.10 Model Validation

Before the model is used in the optimization, it is compared against the published diesel-engine ORC results of Yang et al. (2015). The study by Yang et al. (2015) is used as the validation reference because it uses the same main heat-transfer correlations as the present model. First, both use the same three correlations Wang et al. (Wang et al., 2000), Gnielinski (1976), and Liu–Winterton (1991) therefore the comparison mainly checks the implementation, not the choice of correlations. Second, both use the same performance indicators power output per unit heat-exchanger area POPA (kW/m²) and total exergy destruction rate EDR (kW). Third, both apply a subcritical non-superheated ORC with first- and second-law analysis. Fourth, Yang et al. (2015) report a full Pareto front in POPA–EDR space, which allows the comparison to go beyond a single operating point.

Compared with Yang et al. (2015), the present work applies this modelling approach to a lower-temperature mGT exhaust source, evaluates multiple hydrocarbons working fluids, uses heat-exchanger geometry as decision variables, adds SIC as a third objective, and uses NSGA-II with TOPSIS for decision-making.

3.10.1 Parameter Settings for the Validation Run

For the validation, the main mGT model settings are replaced with those of the diesel-engine ORC case from Yang et al. (2015). This is not a separate design study. The working fluid, exhaust conditions, geometry, and decision variables are only changed for this comparison. The main model settings are restored afterwards. The two performance indicators used by both models are:

$$POPA = \frac{\mathrm{P}net}{A_{\mathrm{popa}}} \quad [\mathrm{kW/m^2}] \tag{3.50}$$

$$EDR = TED \quad [\mathrm{kW}] \tag{3.51}$$

Table 3.1 lists all settings applied for the validation run.

Table 3.1: Parameter settings for the Yang et al. [9] validation run.

Parameter	Main model	Validation run
Working fluid	4 Organic fluids	R245fa
Exhaust inlet temperature	513 K	667 K
Exhaust mass flow rate	0.9 kg/s	0.36 kg/s
Acid dew-point limit	343 K	393 K
Ambient temperature	284.15 K	291.15 K
Tube outer/inner diameter	12.7/10.7 mm	25/20 mm
Fin thickness	0.3 mm	1.0 mm
Pump isentropic efficiency	0.70	0.65
Design variables	Pe, Pc, $\dot{m}_o$, p, S, N_p, N_r	Pe and T_{cond}

In the validation run, the working-fluid mass flow rate is not optimized directly.

3.10.2 Comparison Scope and Acceptance Criteria

Yang et al. (2015) did not include pipe pressure drops or component heat losses. The present model does include condenser fan power, generator conversion loss, and gas-side blower penalties. To account for this, two comparison levels are used. The detailed model keeps all auxiliary losses. The gross model removes them to match the scope of Yang et al. (2015).

For the gross comparison, the target relative errors are below 5 % for net power and thermal efficiency, and below 10 % for EDR. The Pareto front comparison checks that both models show the same trade-off direction in POPA–EDR space. Small differences due to the different property libraries (CoolProp (Bell et al., 2014) versus REFPROP (Lemmon et al., 2018)) are expected. The validation results are presented and discussed in Section 5.1.

3.11 Economic and Environmental Post-Processing

After TOPSIS selects the best design, a set of additional indicators are calculated to show its practical value. These are not objective functions and do not influence the optimization or the TOPSIS ranking. They are calculated from the final selected design.

Annual electricity output is the product of net power and assumed operating hours hop = 8,000 h/yr, based on continuous mGT operation:

$$E_{\mathrm{ORC}} = \mathrm{P}net h_{\mathrm{op}} \tag{3.52}$$

The ORC thermal efficiency compares net electrical output to the total heat absorbed in the preheater and evaporator:

$$\eta_{\mathrm{ORC}} = \frac{\mathrm{P}net}{\dot{Q}_{\mathrm{pre}} + \dot{Q}_{\mathrm{eva}}} \tag{3.53}$$

Avoided CO_2 emissions are estimated by assuming the ORC output replaces Belgian grid electricity, using an emission factor of EF_{grid} = 0.13173 kg CO_2e/kWh (AIB Belgian residual mix 2024 (European Environment Agency, 2024)):

$$CO_{2,\mathrm{avoided}} = \mathrm{P}net h_{\mathrm{op}} EF_{\mathrm{grid}} \tag{3.54}$$

Capital expenditure is specific investment cost multiplied by net power:

$$CAPEX = SIC \times \mathrm{P}net \tag{3.55}$$

To calculate the simple payback period, the following assumptions are used. Electricity revenue grows at r_e = 3 %/yr and O&M cost, set at 3 % of CAPEX following ORC waste-heat-recovery practice (Quoilin et al., 2013), grows at inflation rate i = 2 %/yr:

$$\sum_{y=1}^{N} \left[P_{\mathrm{net}} h_{\mathrm{op}} C_e (1 + r_e)^{y-1} - 0.03\, CAPEX (1 + i)^{y-1} \right] - CAPEX \geq 0 \tag{3.56}$$

The Belgian household electricity price C_e = 0.3499 €/kWh (Eurostat H2 2025 (Eurostat, 2025)) is used as the revenue estimate.

4 Optimization and Decision-Making Framework

Chapter 3 developed the ORC model that calculates Pnet, TED, and SIC for each feasible design. This chapter explains how these outputs are used in the optimization and in the final design selection step. It covers the decision variables and their bounds, the three objective functions, how constraints are handled, the NSGA-II settings, the Pareto filtering step, and the TOPSIS ranking.

The problem needs more than one objective because the design targets do not all improve in the same direction. A larger heat-transfer area recovers more heat and reduces exergy destruction, but it raises cost and gas-side pressure drop. A lower condensation pressure can increase turbine work, but for some fluids it leads to sub-atmospheric condenser operation. A higher evaporation pressure increases the turbine enthalpy drop but can reduce the boiler temperature difference and make the heat exchanger longer. Because these effects pull against each other, there is no single best design. Three objectives are therefore used maximize Pnet, minimize TED, and minimize SIC and NSGA-II (Deb et al., 2002) is applied to find the Pareto front.

NSGA-II is chosen because it finds a set of non-dominated solutions in one run without combining the objectives into a single weighted value. This is useful since the balance between cost, exergy, and power is easier to analyses the trend once the full Pareto front is available.

Figure 4.1 shows the calculation flow. NSGA-II creates candidate designs and sends each one to the ORC model, which checks feasibility, solves the thermodynamic cycle, sizes the two-zone heat exchanger, applies gas-side pressure-drop penalties, and returns the three objective values. NSGA-II ranks the population by non-dominated sorting and crowding distance, then applies tournament selection, crossover, and mutation to create the next generation. After the final generation, the Pareto front is identified and TOPSIS selects one design for working fluid.

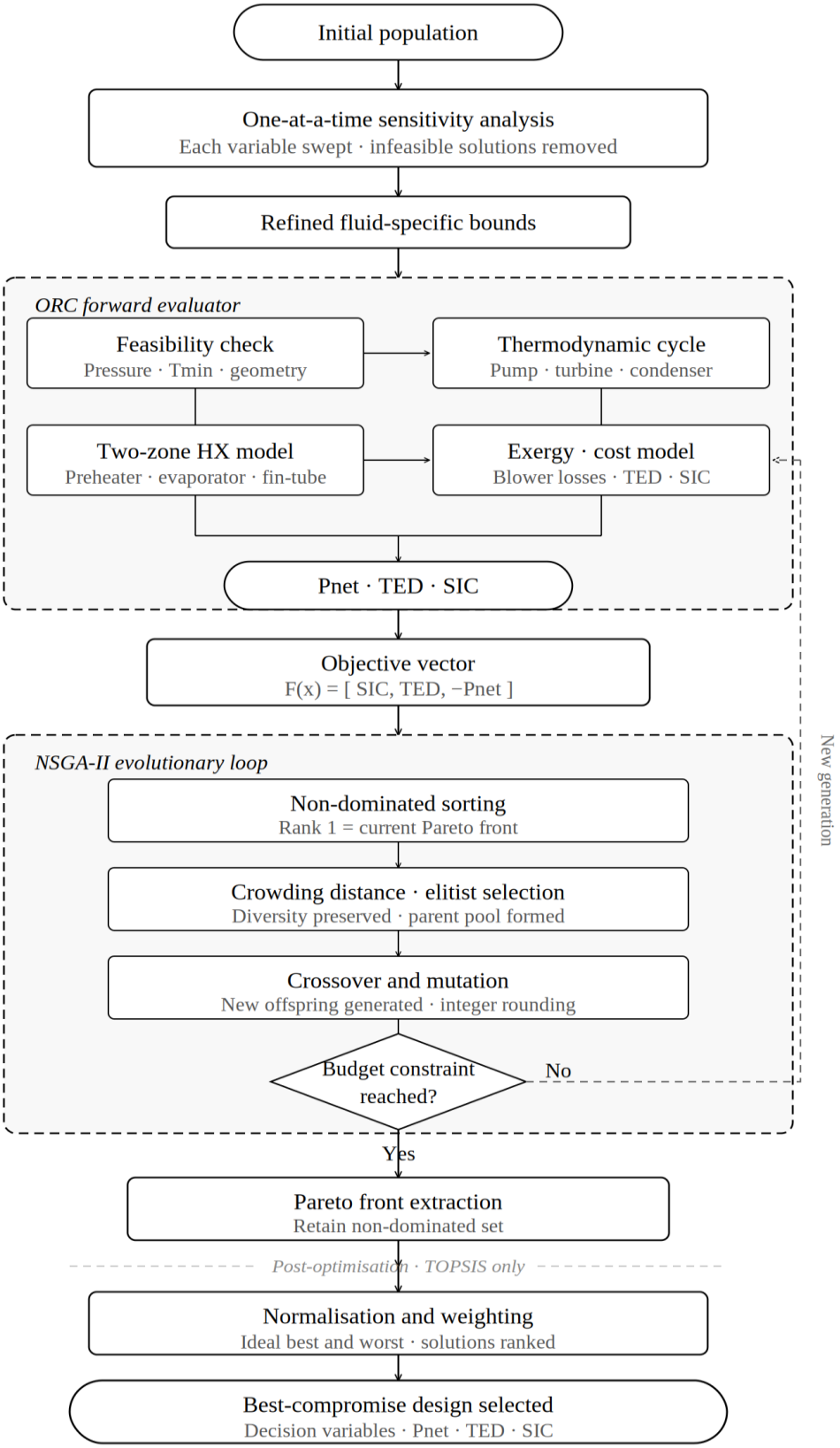

Figure 4.1: NSGA-II and TOPSIS calculation workflow. The inner loop links the evolutionary operators with the ORC model. TOPSIS is applied only to the final non-dominated set.

4.1 Decision Variables and Search Space

The seven decision variables are evaporation pressure Pe, condensation pressure Pc, working-fluid mass flow rate $\dot{m}_o$, fin pitch p, tube spacing S, number of parallel tubes per row N_p, and number of tube rows N_r. These variables affect the thermodynamic cycle, heat-transfer area, gas-side pressure drop, exergy destruction, and equipment cost. Table 4.1 gives the initial search bounds used before fluid-specific OAT refinement.

Table 4.1: Global decision-variable bound structure used before fluid-specific OAT refinement.

Variable	Lower bound	Upper bound	Type
Pe	400 kPa	$0.95 \times P_{crit}$	Continuous
Pc	P_{sat}(50 °C)	200 kPa	Continuous
$\dot{m}_o$ (kg/s)	0.10	0.30	Continuous
p (mm)	2.0	9.0	Continuous
S (mm)	24.0	40.0	Continuous
N_p	5	40	Integer
N_r	2	8	Integer

The bounds were set from physical limits, operating requirements, and preliminary model checks. The upper bound for Pe is $0.95 \times P_{crit}$ of the working fluid, which keeps the cycle subcritical and within the valid range of the boiling correlations. The upper bound for Pc is 200 kPa, above which the turbine pressure ratio becomes too small for useful power recovery. The mass flow rate is limited to 0.30 kg/s based on preliminary heat-balance checks with the 240 °C exhaust above this value, many designs fail the pinch-point or gas-outlet-temperature limits. Fin pitch (2.0–9.0 mm) and tube spacing (24.0–40.0 mm) are within the practical range for compact gas-to-liquid heat exchangers reported in the literature (Yang et al., 2015; Maalouf et al., 2012). N_p is capped at 40 to avoid an impractically wide exchanger, and N_r is capped at 8 to avoid excessive gas-side pressure drop; preliminary checks showed only small gains in Pnet beyond these values while cost and pressure drop continued to rise.

N_p and N_r are integer variables, but NSGA-II works with continuous values. They are treated as continuous variables during crossover and mutation, then rounded to the

nearest integer before being used in the model calculation. This implementation keeps the genetic operators unchanged while ensuring that only integer tube counts and row numbers are evaluated.

Before the main NSGA-II run, a one-at-a-time (OAT) sensitivity analysis is carried out by changing one variable at a time while holding the others fixed. This identifies the useful search range for each fluid and avoids spending evaluations in clearly infeasible or low-performance regions.

4.2 Objective Functions

The three objectives are Pnet from Eq. (3.10), TED from Eq. (3.45), and SIC from Eq. (3.49). They each measure a different aspect of ORC performance and partly conflict with each other.

Pnet is the net electrical output after subtracting pump power, condenser fan power, and gas-side pressure-drop penalties. It is the main measure of useful energy recovery. SIC is the specific investment cost in €/kW and stops the optimizer from selecting over-sized heat exchangers that give only small power gains at high cost. Quoilin et al. (2013) showed that at sub-100 kW scale, heat exchangers and expanders dominate total system cost, making SIC a sensitive indicator at this scale. TED is the total exergy destruction across all ORC components, and it reflects the second-law quality of the design. Nami et al. (2018) found that the evaporator accounts for the largest share of exergy destruction in gas-turbine exhaust ORC systems, so TED is a useful second-law objective at this exhaust temperature.

Because NSGA-II is implemented in minimization form, the objective vector is written as:

$$\mathrm{F}(\mathrm{x}) = [\mathrm{SIC}(\mathrm{x}),\ \mathrm{TED}(\mathrm{x}),\ -\mathrm{P}net(\mathrm{x})] \tag{4.1}$$

where x is the seven-variable design vector. Minimizing −Pnet is equivalent to maximizing Pnet.

4.3 Constraint Handling

The eight feasibility conditions from Section 3.9 are checked inside the ORC model. If any condition fails, the model returns penalty objective values high SIC, high TED, and low Pnet without completing the remaining calculations. This gives infeasible candidates a poor non-domination rank and they are dropped during selection.

A penalty approach is used because some feasibility checks depend on results from the ORC model itself. The pinch point, gas outlet temperature, exergy balance, and NTU iteration are all calculated during model evaluation. There is no straightforward way to correct an infeasible design before evaluation, so penalty rejection is simpler and consistent with common constraint-handling practice in evolutionary algorithms (Deb et al., 2002).

4.4 NSGA-II Implementation

NSGA-II is run through the RHEIA framework (Coppitters et al., 2020), which handles population management and genetic operators. The ORC model is connected as an external evaluator. Three features of NSGA-II are important here. Non-dominated sorting separates the population into ranked layers, with Rank 1 being the current Pareto-front estimate. Elitist selection keeps the best solutions from one generation to the next. Crowding distance spreads solutions across the front so that low-cost, low-exergy-destruction, and high-power designs all stay in the population.

The settings used are population size 20, evaluation budget 800, crossover probability 0.90, mutation probability 0.10 per variable, and distribution index $\eta = 0.20$. The starting population is seeded by Latin Hypercube Sampling within the OAT-refined bounds, giving a broad spread of initial designs.

The same settings are applied separately to n-pentane, cyclopentane, n-hexane, and n-heptane, each using its own OAT-refined pressure bounds. The only thing that differs between fluids is the saturation-dependent pressure limits. Differences in results therefore come from fluid properties and heat-transfer behavior, not from the optimization setup.

4.5 Pareto Filtering and TOPSIS Ranking

After the final generation, penalty solutions are removed and the non-dominated set is identified by comparing all feasible designs. A design stays on the Pareto front if no other feasible design has lower SIC, lower TED, and higher Pnet at the same time.

TOPSIS (Hwang & Yoon, 1981) is applied separately to each fluid's Pareto set. The decision matrix is built from the Pareto-front values of SIC, TED, and Pnet, then normalized

by the Euclidean norm of each column to remove differences in units and scale. The weights used are wSIC = 0.40, wPnet = 0.35, and wTED = 0.25.

These weights reflect the priorities of a small-scale mGT waste-heat recovery system. SIC gets the highest weight (0.40) because cost per kW is the main practical constraint for small ORC systems (Quoilin et al., 2013). A design that is too expensive per kilowatt is unlikely to be installed even if it performs well thermodynamically. Pnet gets 0.35 because recovering useful electricity is the primary purpose of the system. TED gets 0.25 as a thermodynamic quality indicator which is important for comparing designs, but less directly tied to project economics than cost or power.

TOPSIS defines an ideal best point which indicate the lowest SIC, lowest TED, and highest Pnet in the Pareto set and an ideal worst point with the opposite values. Each design is scored by its closeness coefficient:

$$CC_i = \frac{D_i^-}{D_i^+ + D_i^-} \tag{4.2}$$

where D_i^+ and D_i^- are the weighted Euclidean distances to the ideal best and ideal worst points. The design with the highest CC_i is selected as the best compromise design for that fluid.

5 Results and Discussion

This chapter presents the results of the ORC model and optimization. It starts with model validation to check the calculation method before applying it to the working fluids. The chapter then discusses fluid screening, OAT sensitivity analysis, NSGA-II Pareto fronts, and TOPSIS selection. These steps show how the working fluids behave and how the main decision variables affect net power, exergy destruction, and specific investment cost. The selected n-pentane design is then examined using the T–s diagram, the three-dimensional Pareto front, the component exergy split, and the economic and environmental indicators.

5.1 Model Validation

Before the optimization results are presented, the ORC model is compared with the published study of Yang et al. (2015). This check is done to make sure the model gives reasonable results before it is used for the four working fluids. The comparison uses POPA and EDR, because these are the main indicators reported by Yang et al. (2015). The validation setup and acceptance criteria are described in Section 3.10. The results fall within these limits, and the model is accepted as suitable for the main mGT exhaust optimization.

The comparison is made at an evaporation pressure of 2.4 MPa and a condensation temperature of 298.15 K. Two versions of the present model are used. The first version removes the main auxiliary losses to match the assumptions of Yang et al. (2015). The second version is the full model used in this thesis, which includes condenser fan power, generator conversion loss, and gas-side pressure-drop penalties.

Table 5.1 shows the results. With Yang-compatible assumptions, the model gives 13.61 kW net power, compared with 13.84 kW in Yang et al. (2015) a difference of only 1.6 %. POPA is also close: 0.746 kW/m² for the present model and 0.740 kW/m² in the reference. When the full detailed model is used, the differences are larger because of the extra losses. Net power drops to 9.20 kW and thermal efficiency to 8.77 %. This shows that the core ORC cycle calculation matches the published result well, and the larger differences in the detailed case come from the additional loss terms that Yang et al. (2015) did not include.

Table 5.1: Validation comparison with Yang et al. (2015).

Parameter	Unit	Yang et al. [9]	compati-ble model	Error	Detailed model	Error
POPA	kW/m²	0.740	0.746	+0.8 %	0.680	−8.1 %
TED	kW	33.10	34.12	+3.1 %	35.72	+7.9 %
Pnet	kW	13.84	13.61	−1.6 %	9.20	−33.5 %
Efficiency	%	13.33	12.98	−2.6 %	8.77	−34.2 %

Figure 5.1 compares the POPA–EDR Pareto fronts. The detailed model gives lower POPA and higher EDR than Yang et al. (2015), which is expected given the extra losses included. Both fronts show the same trade-off direction: as POPA increases, EDR also increases. The present model reproduces the same trade-off behavior as the reference study. The validation results are within the acceptance criteria. The model is therefore considered suitable for the main mGT exhaust optimization.

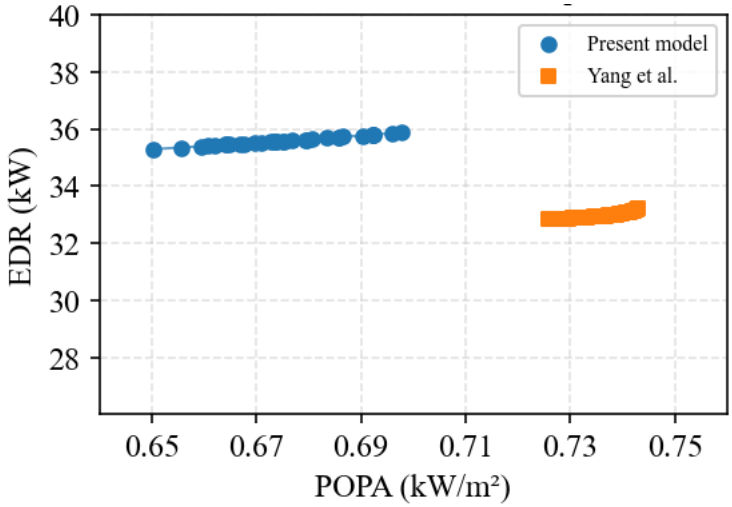

Figure 5.1: POPA–EDR Pareto-front comparison between the present model with Yang et al. (2015).

5.2 Working-Fluid Screening and Selection

The ORC model uses saturated vapour at the turbine inlet with no superheating. Expansion must therefore remain in the vapor region throughout, which restricts candidates

to dry or isentropic fluids whose saturated-vapor curves slope positively in the T–s diagram.

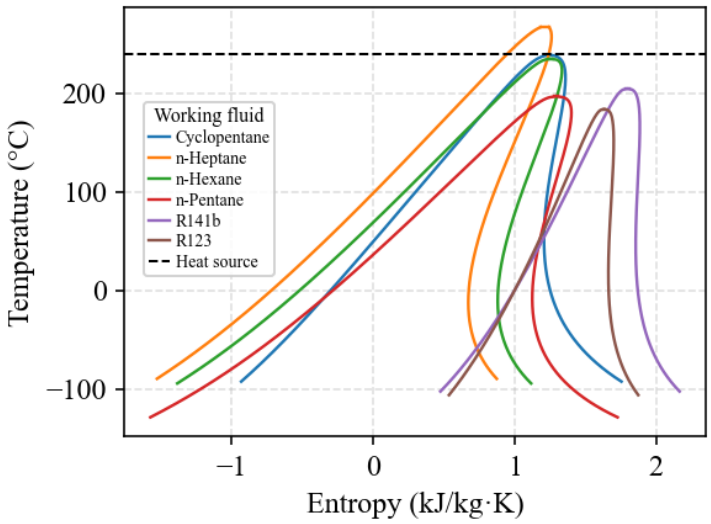

Figure 5.2: Temperature–entropy saturation diagram of the six candidate fluids against the 240 °C mGT exhaust source temperature.

Figure 5.2 shows that n-pentane, cyclopentane, n-hexane, and n-heptane all have suitable saturated-vapor curves and are kept for optimization. R141b and R123 are removed because of their ODP and regulatory restrictions, as discussed in Section 2.2.

The T–s diagram also helps explain why the four fluids behave differently in the optimization. Cyclopentane and n-hexane have critical temperatures of 238.6 °C and 234.7 °C, close to the 240 °C exhaust source. This allows them to evaporate near the source temperature, which reduces the boiler temperature mismatch and the exergy destruction identified by Nami et al. (2018) as the main ORC irreversibility. n-Pentane (critical temperature 196.6 °C) works at higher evaporation pressure with an above-atmospheric condensation pressure. This leads to good power and cost performance but requires a longer liquid preheating zone before evaporation. n-Heptane (critical temperature 267.0 °C) can match the source temperature, but it needs near-vacuum condensation, which can create sealing difficulties and higher condenser cost.

5.3 Sensitivity Analysis

A one-at-a-time (OAT) sensitivity analysis was done before the NSGA-II run. Each variable was changed one at a time while the others were held at representative values. The aim

was to find the useful search range for each fluid and avoid spending the 800 model evaluations in regions that are clearly infeasible or give poor objective values.

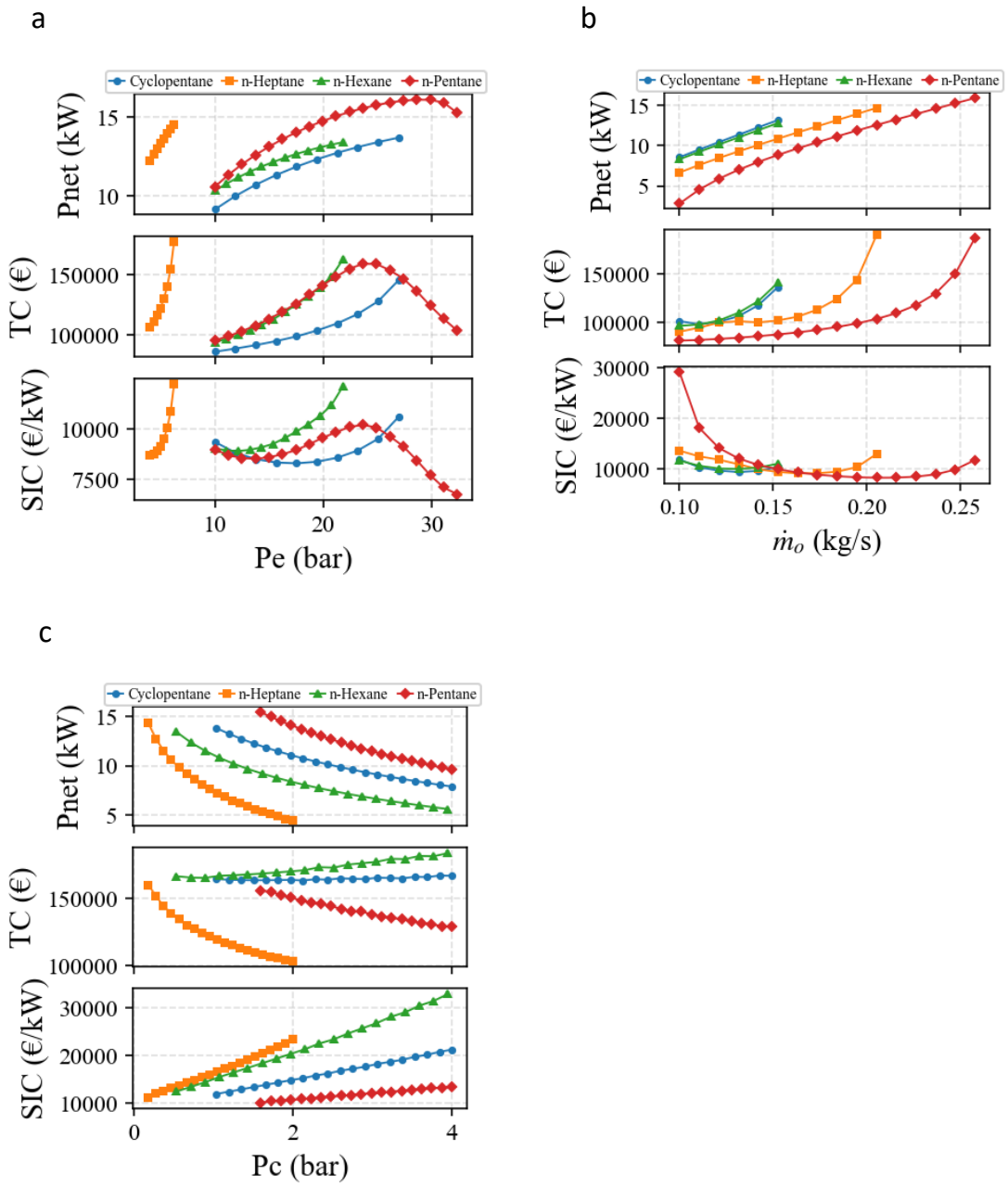

Figure 5.3: OAT sensitivity of the four retained hydrocarbons to (a) working-fluid mass flow rate $\dot{m}_o$, (b) evaporation pressure Pe, and (c) condensation pressure Pc, showing the corresponding effect on Pnet, total cost TC, and SIC.

Figure 5.3 shows that Pe, Pc, and $\dot{m}_o$ have the strongest effect on the objectives. The geometric variables mainly affect cost and gas-side pressure drop and are shown in Appendix B.

For the mass-flow-rate sweep, SIC first drops and then rises for all four fluids. At low $\dot{m}_o$, raising mass flow rate increases Pnet faster than cost, therefore SIC falls. After a certain

point, more heat-exchanger areas are needed but the power gain becomes smaller, for this reason SIC rises again. The SIC minimum is near 0.20 kg/s for n-pentane and around 0.13 kg/s for cyclopentane and n-hexane. TED increases steadily with mass flow rate because more heat is transferred through the components.

For the evaporation-pressure sweep, n-pentane responds most strongly. Higher Pe increases the turbine pressure ratio and vapor density at the same time therefore the evaporator area per unit duty falls while Pnet grows and SIC drops. Cyclopentane and n-hexane show a smaller improvement at high Pe because they get close to the critical region, where the boiler temperature difference shrinks and the heat exchanger must grow to absorb the same duty. n-Heptane shows very little response because its useful pressure range is narrow.

For the condensation-pressure sweep, Pnet reduces as turbine outlet pressure rises for all fluids.

Table 5.2: Fluid-specific refined NSGA-II bounds from the OAT sensitivity analysis.

Fluid	Pe (bar)	Pc (bar)	$\dot{m}_o$ (kg/s)	p (mm)	S (mm)	N_p	N_r
n-Pentane	24–30	1.6–3.0	0.20–0.26	3–6	30–40	18–40	3–8
Cyclopentane	17–28	1.04–3.0	0.13–0.18	3–5	32–40	30–40	4–8
n-Hexane	12–22	0.54–3.0	0.13–0.18	3–6	30–40	25–40	4–8
n-Heptane	4–7	0.19–0.80	0.16–0.22	3–6	30–40	16–40	3–8

The bounds are different for each fluid. n-Pentane uses the highest evaporation pressure and mass flow rate because its best designs use high turbine pressure ratios at above-atmospheric condensation. Cyclopentane and n-hexane operate at lower mass flow rates because they match the source temperature better. n-Heptane is limited to a narrow low-pressure range because its high critical temperature forces very low condensation pressures to keep a useful expansion ratio.

5.4 Pareto-Front Analysis

NSGA-II was run separately for each working fluid using the refined bounds from Table 5.2. Each run used 800 model evaluations and took about 3.2 hours. After the run, the non-dominated solutions were identified as the Pareto front.

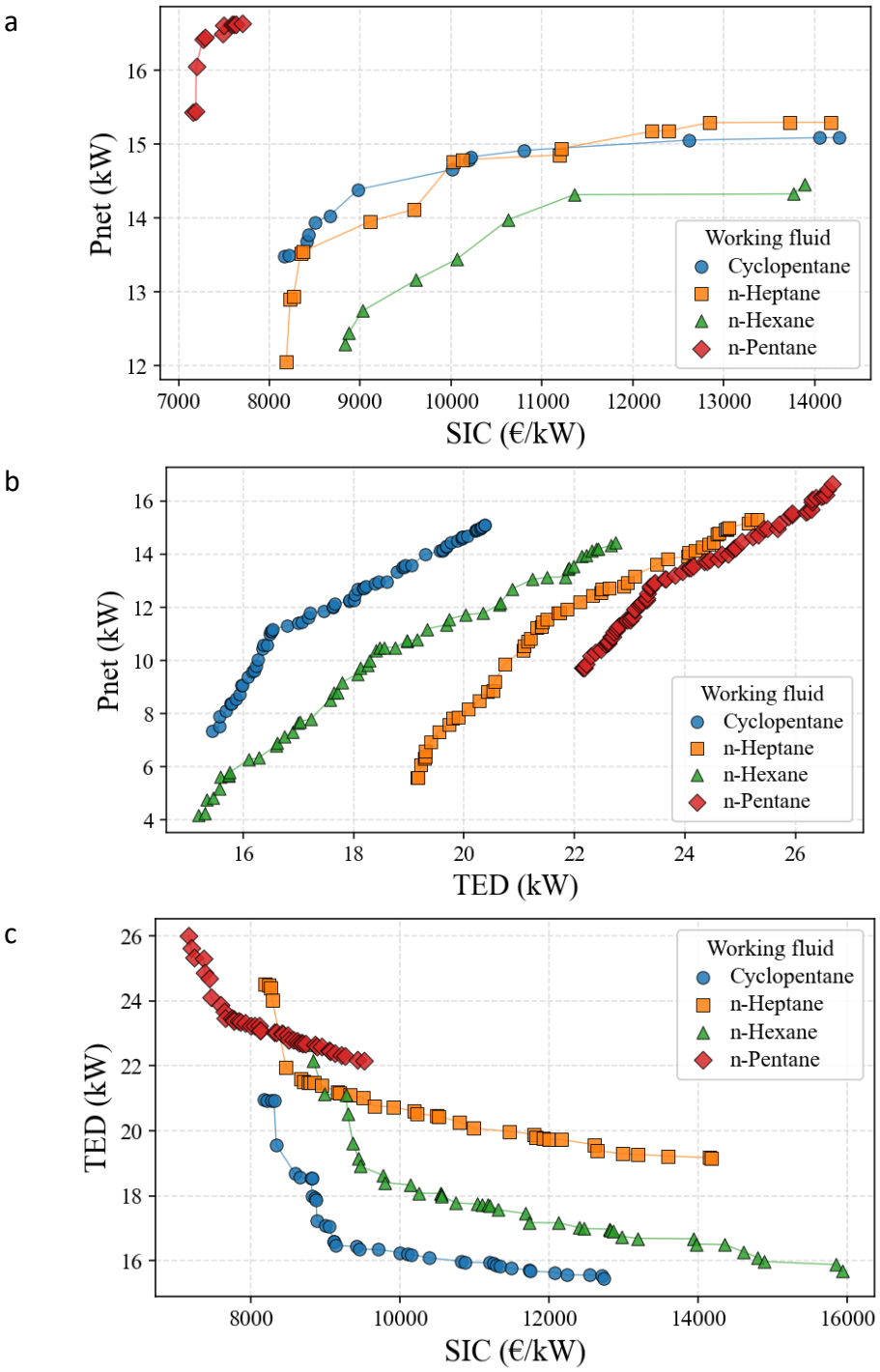

Figure 5.4: Two-dimensional projections of the NSGA-II Pareto front (a) Pnet–SIC, (b) Pnet–TED, and (c) TED–SIC.

In the Pnet–SIC graph n-pentane is clearly separated from the other three fluids. Its Pareto front covers SIC from €7,159 to €7,700/kW and Pnet from 15.43 to 16.63 kW. The range is narrow only €541/kW over 1.2 kW of power, and no solution from the other fluids reaches a SIC below €8,169/kW. The near-flat curve means that extra heat-exchanger investment gives proportional power gains without a large cost increase. As Pe rises, vapor density increases and evaporator volume per unit duty falls, so total cost stays stable while Pnet continues to grow. The cost advantage comes with a higher TED: n-pentane must heat the working fluid as single-phase liquid from about 50 °C to 188.6 °C before boiling starts, so 79 % of the total boiler duty falls into a zone where the fluid and exhaust temperatures are far apart. This accumulates exergy destruction regardless of heat-exchanger size, which is why n-pentane's entire Pareto curve sits in the highest TED band in the Pnet–TED projection.

Cyclopentane behaves differently. In the Pnet–SIC graph its curve is long and curved steep at the low-SIC end and flattening toward the maximum Pnet. This happens because raising Pe toward its critical temperature of 238.6 °C narrows the boiler temperature difference and forces the heat exchanger to grow steeply. A €6,100/kW cost spread gives only a 1.6 kW Pnet gain, so extra area gives diminishing returns at the high-Pe end. In the Pnet–TED graph cyclopentane stays in the lowest TED band at all power levels (TED from 15.44 to 20.97 kW). Its balanced heat-duty split keeps boiler entropy generation consistently lower than any other fluid at a given Pnet. In the TED–SIC graph its curve is nearly diagonal, showing a clear trade-off where more area reduces TED and raises SIC at roughly constant Pnet.

n-Hexane reaches the lowest TED in the study at 15.19 kW, but only at Pnet of about 4.17 kW and SIC of €19,238/kW. Its curve runs into the high-SIC, low-power corner, which means TED-minimizing designs are too expensive to be practical. n-Heptane reaches Pnet of about 15.30 kW at SIC up to €14,183/kW but carries TED of 25.31 kW at that point. Its near-vacuum condensation constraint limits the achievable TED floor to about 19.15 kW within the search bounds. Moving from minimum TED to maximum Pnet raises SIC substantially while reducing TED only a little, which shows the limitation comes from the condensation pressure constraint, not from insufficient heat-exchanger area.

The three pareto fronts together show that n-pentane is the stronger option when cost and power are the main priorities, and cyclopentane is stronger when thermodynamic quality matters more.

5.5 TOPSIS Best-Compromise Solution

TOPSIS was applied to the final Pareto set of each fluid using the weights from Section 4.5: wSIC = 0.40, wPnet = 0.35, wTED = 0.25. Cost gets the highest weight because it is the main barrier to adoption at sub-100 kW scale (Quoilin et al., 2013). Net power gets the second weight because recovering useful electricity is the main purpose of the ORC. TED is kept as a thermodynamic quality indicator but gets a lower weight because project decisions at this scale are more strongly driven by cost and power.

Table 5.3: TOPSIS-selected operating variables.

Fluid	Pe (bar)	Pc (bar)	$\dot{m}_o$ (kg/s)	p (mm)	S (mm)	N_p	N_r
n-Pentane	29.83	1.61	0.250	3.3	38	27	4
Cyclopentane	21.63	1.05	0.175	3.4	32	31	6
n-Heptane	6.45	0.19	0.192	3.3	33	20	5
n-Hexane	20.17	0.57	0.167	3.3	36	27	6

Table 5.4: TOPSIS-selected performance indicators.

Fluid	Pnet (kW)	TED (kW)	SIC (€/kW)	Total cost (€)
n-Pentane	15.96	26.52	7,169	114,390
Cyclopentane	13.94	20.58	8,498	118,470
n-Heptane	13.96	24.13	9,107	127,174
n-Hexane	13.45	21.90	10,084	135,630

The heat-duty split explains n-pentane's higher TED. At Pe = 29.83 bar, n-pentane boils at 188.6 °C but condensates near 50 °C. As a result, 102.5 kW of the 130.3 kW total boiler duty about 79 % goes into single-phase liquid preheating over a 138 K temperature span. In this zone the working fluid and exhaust temperatures are far apart, which generates entropy. This is the main cause of the elevated TED, not the evaporation pressure level. Cyclopentane's more balanced split (55.7 kW preheater, 41.9 kW evaporator) gives better source matching and explains its much lower TED.

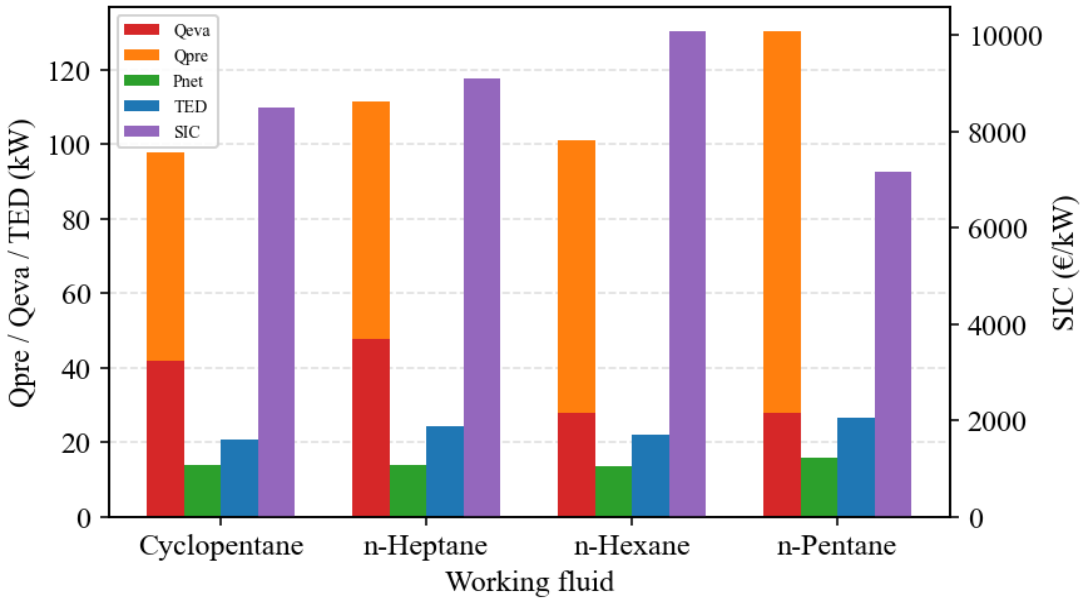

Figure 5.5: TOPSIS best-compromise results for the four working fluids.

Cyclopentane gives the lowest practical TED and would be the better choice if exergy quality is more important than cost. A weight sensitivity check confirms that n-pentane stays preferred under cost- and power-dominant weighting, but cyclopentane becomes the better option when TED gets the dominant weight. At that point, cyclopentane gives 87 % of n-pentane's Pnet at 19 % higher SIC. n-Pentane is taken forward for the detailed assessment.

5.6 Further Assessment of the Selected Design

The selected design is the TOPSIS-ranked n-pentane case Pe = 29.83 bar, Pc = 1.61 bar, $\dot{m}_o$ = 0.250 kg/s, p = 3.3 mm, S = 38 mm, N_p = 27, N_r = 4. It is examined using the T–s diagram, the three-dimensional Pareto front, and the component exergy split.

The T–s diagram confirms the cycle is physically valid. The working fluid is pumped from State 1 (saturated liquid) to State 2, heated as single-phase liquid to the saturated-liquid boundary at State 2', evaporated to saturated vapor at State 3 (188.6 °C), expanded to State 4 (about 105 °C, superheated), and condensed back to State 1.

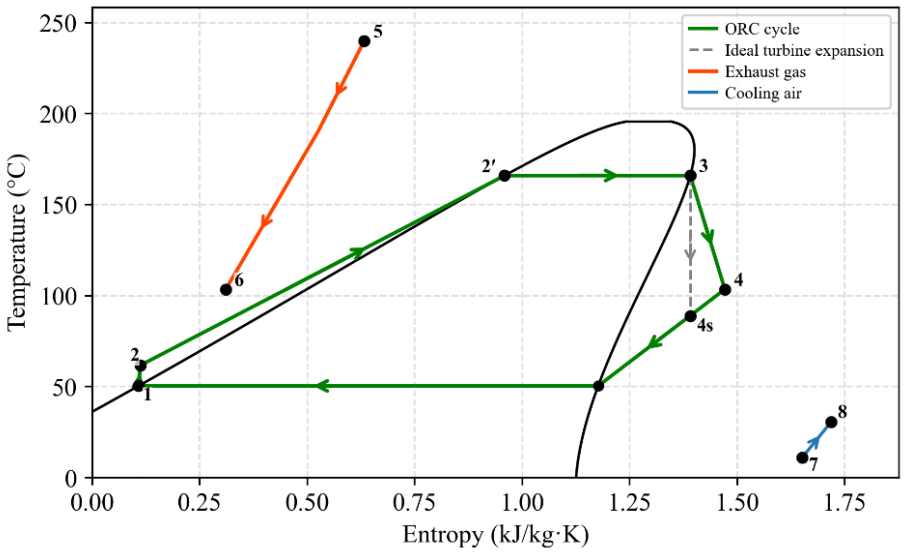

Figure 5.6: T–s diagram of the TOPSIS-selected n-pentane ORC cycle with labelled state points.

The actual turbine specific work of about 76.4 kJ/kg against the isentropic value of 109.2 kJ/kg confirms the 70 % turbine efficiency. The exhaust leaves the preheater at 101.2 °C, which is above the 70 °C acid dew-point limit, and the condenser rejects 112.9 kW to cooling air.

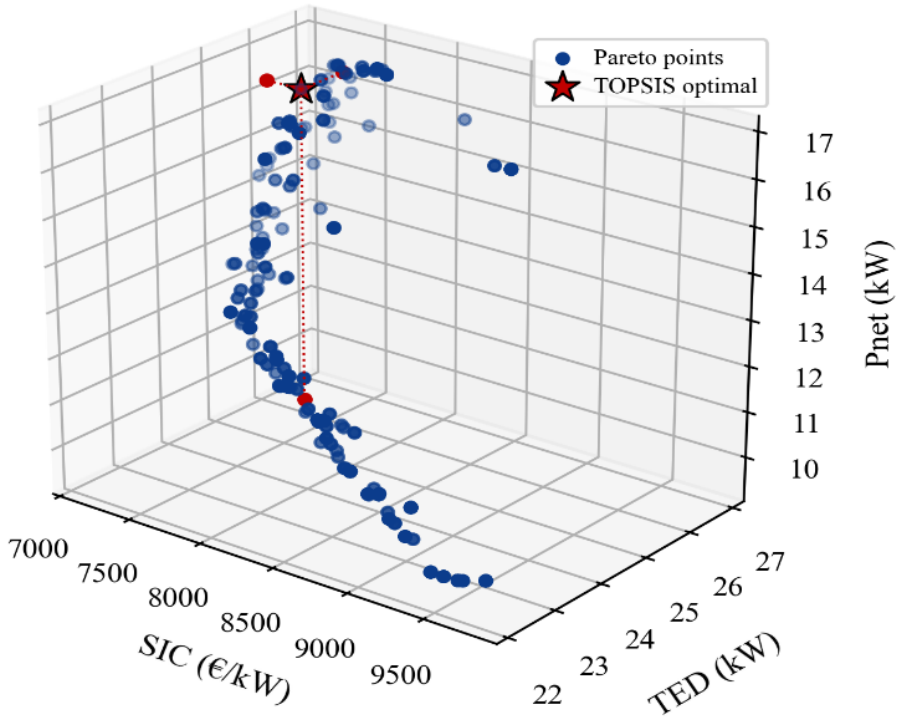

Figure 5.7: Three-dimensional n-pentane Pareto front with the TOPSIS-selected solution (red star) highlighted.

Figure 5.7 shows that TOPSIS design is a member of the non-dominated set. It is shown at the high-Pnet, low-SIC end of the three-dimensional front. Moving toward lower TED from this point would reduce Pnet and raise SIC, which does not match the TOPSIS weights. The TED of 26.52 kW puts it near the high-TED end of the n-pentane front.

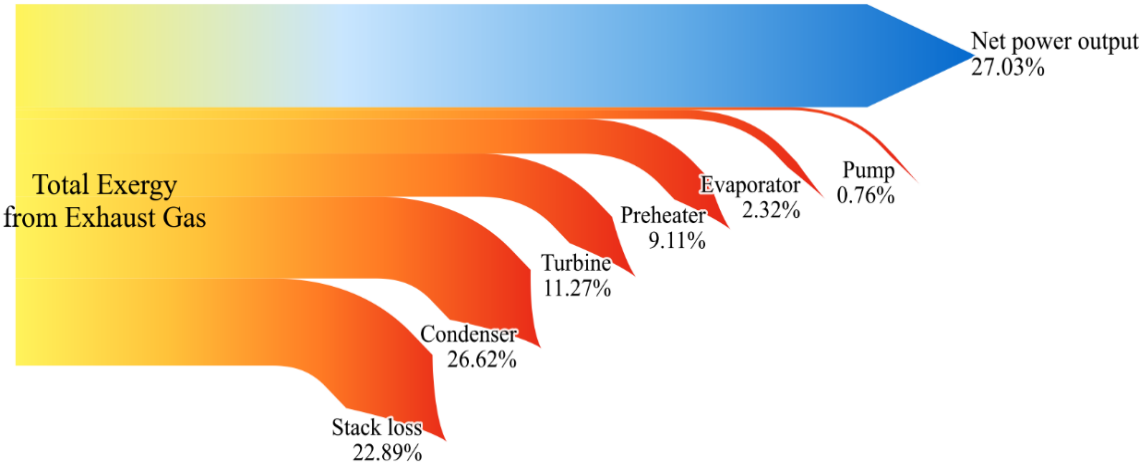

Figure 5.8: Exergy split for the selected n-pentane design, normalized to total exhaust-gas exergy input.

Of the 60.89 kW of available exhaust-gas exergy, 27.03 % is converted to net electrical power. The condenser (26.62 %) and stack loss (22.89 %) together account for nearly half the input. The condenser rejects heat across a log-mean temperature difference of 28.4 K, and the stack carries residual exergy that cannot be recovered without violating the pinch-point or acid dew-point constraints. These are structural limits set by the air-cooled condenser and the minimum stack temperature. The turbine accounts for 11.27 % of exergy destruction, the preheater for 9.11 % (from the 138 K liquid heating span), the evaporator for 2.32 % (small because n-pentane at 29.83 bar boils only 51 K below the exhaust inlet), and the pump for 0.76 %.

The thermal efficiency is 12.25 % against a total boiler heat input of 130.3 kW. This is within the expected range for small ORC systems using a 200–250 °C heat source (Quoilin et al., 2013; Tartère & Astolfi, 2017). The exergy split shows that the largest improvement opportunities are in the condenser and stack losses, but reducing these would need larger heat-exchanger area and higher cost. This is the same cost–power–exergy trade-off shown by the Pareto fronts.

5.7 Economic and Environmental Assessment

The economic and environmental indicators are calculated after the TOPSIS selection. They are not objective functions and did not affect the optimization or the TOPSIS ranking. The selected n-pentane design has Pnet = 15.96 kW and CAPEX = €114,390. The assumptions are Belgian household electricity price €0.3499/kWh (Eurostat, 2025), grid emission factor 0.13173 kg CO_2e/kWh (European Environment Agency, 2024), and 8,000 operating hours per year.

The system produces 127.7 MWh/yr. Displacing this output avoids about 16.8 tCO_2e/yr. The modest figure reflects Belgium's already low-carbon electricity mix.

First-year electricity revenue is €44,675. After O&M costs of 3 % of CAPEX (€3,432), the net first-year cash inflow is about €41,244. With revenue growing at r_e = 3 %/yr and O&M at i = 2 %/yr, the cumulative cash flow turns positive in year 3, giving a payback of about 2.7 years. The result is therefore a favorable estimate, not a guaranteed industrial return.

The cyclopentane TOPSIS design (Pnet = 13.94 kW, SIC = €8,498/kW) produces about 111.5 MWh/yr and has an estimated payback of about 3.2 years under the same assumptions. The 22 % reduction in TED compared with n-pentane comes at the cost of about six additional months of payback. Overall, n-pentane is the better choice when cost and power matter most, and cyclopentane is better when exergy quality is the main priority.

6 Conclusion and future work

6.1 Conclusions

This thesis investigated a subcritical ORC for recovering electricity from the post-recuperator exhaust of a 240 °C micro gas turbine. The work focused on selecting a working fluid and operating design that gives a good balance between net power output, total exergy destruction, and specific investment cost. To do this, a three-objective NSGA-II optimization method was combined with a two-zone finned-tube heat-exchanger model and TOPSIS decision-making.

Six candidate fluids were first screened. R141b and R123 were removed because of their ODP and regulatory restrictions. The four retained fluids were n-pentane, cyclopentane, n-hexane, and n-heptane. All four meet the dry-fluid requirement for saturated-vapor turbine inlet operation. Cyclopentane and n-hexane match the 240 °C exhaust source better and therefore give lower exergy destruction. n-Pentane works at higher evaporation pressure and has above-atmospheric condensation pressure, which is more practical. n-Heptane needs near-vacuum condensation, which makes it less attractive.

The OAT sensitivity analysis showed that evaporation pressure, condensation pressure, and working-fluid mass flow rate have the strongest effect on the results. The geometric variables mainly affect equipment cost and gas-side pressure-drop losses. The OAT results were used to reduce the search space before the NSGA-II runs.

The Pareto fronts showed a clear difference between the fluids. n-Pentane gave the best cost and power performance, with a minimum SIC of €7,159/kW and a maximum Pnet of 16.63 kW. Cyclopentane gave the lowest TED at comparable power levels because of its better thermal match with the exhaust source.

TOPSIS was applied using weights of 0.40 for SIC, 0.35 for Pnet, and 0.25 for TED. With these weights, n-pentane was selected as the final compromise design. The selected points has Pe = 29.83 bar, Pc = 1.608 bar, and $\dot{m}_o$ = 0.2496 kg/s. It gives Pnet = 15.96 kW, SIC = €7,169/kW, and TED = 26.52 kW.

The exergy split showed that the condenser and stack are the largest loss locations, with 26.6 % and 22.9 % of the available exhaust-gas exergy. Turbine losses account for 11.3 %, and preheater irreversibility accounts for 9.1 %. At 8,000 operating hours per year, the

selected n-pentane design produces about 127.7 MWh/yr. Under the Belgian household electricity tariff assumption, it avoids about 16.8 tCO_2e/yr and gives an estimated simple payback of 2.7 years.

Overall, n-pentane is recommended when cost and net power are the main priorities. It gives the lowest SIC, the highest Pnet, and a practical condensation pressure. Cyclopentane remains the better option when lower exergy destruction is more important than minimum cost. The final working-fluid choice therefore depends on the design priority.

6.2 Limitations

The model used in this thesis is a steady-state design-point model. It does not include part-load operation, start-up behaviour, or seasonal changes in ambient temperature. The turbine and pump isentropic efficiencies are fixed at 0.70, so they do not change with pressure ratio, mass flow rate, or working fluid.

The model was checked against published ORC modelling results and component-level correlations from Yang et al. [9], but no experimental validation of the full integrated system was carried out.

The cost calculation uses the Turton et al. [36] purchased-equipment-cost correlations updated to 2024 using CEPCI. It does not include installation, piping, control systems, civil works, commissioning, permitting, or safety equipment. For this reason, SIC should be read as a comparative cost indicator, not as a full project cost.

The payback calculation uses Belgian household electricity prices. This gives a favourable case because these prices include taxes and network charges. The result should not be treated as a guaranteed industrial return.

6.3 Future Work

- Future work should include part-load and annual performance modelling. This would allow the ORC to be tested under changing exhaust temperature, exhaust mass flow rate, and ambient temperature.
- The ORC could also be studied in CHP mode. Adding useful heat recovery from the condenser may make cyclopentane more attractive because of its lower exergy destruction.

- Hydrocarbon safety should be studied before practical use. This should include charge minimisation, ventilation, leak detection, hazardous-zone classification, and compliance with safety standards.
- Finally, experimental validation is recommended. A small test rig using n-pentane under controlled exhaust conditions would help check the predicted Pnet, TED, SIC, and component losses.

Bibliography

A. Tudoroiu-Lakavice and S. Milusheva, Waste Heat Recovery: Potentials, Applications and Recommendations for Better Policies, HEATLEAP Project / COGEN Europe, 2023.

M. Papapetrou, G. Kosmadakis, A. Cipollina, U. La Commare, and G. Micale, 'Industrial waste heat: Estimation of the technically available resource in the EU per industrial sector, temperature level and country,' Applied Thermal Engineering, vol. 138, pp. 207-216, 2018.

E. Cornelis and J. Van Bael, 'How well can the potential of industrial excess heat be estimated?' in ECEEE Industrial Summer Study Proceedings, pp. 199-208, 2016.

T. Tartiere and M. Astolfi, 'A World Overview of the Organic Rankine Cycle Market,' Energy Procedia, vol. 129, pp. 2-9, 2017.

B. F. Tchanche, G. Lambrinos, A. Frangoudakis, and G. Papadakis, 'Low-grade heat conversion into power using organic Rankine cycles: A review of various applications,' Renewable and Sustainable Energy Reviews, vol. 15, no. 8, pp. 3963-3979, 2011.

S. Quoilin, M. Van Den Broek, S. Declaye, P. Dewallef, and V. Lemort, 'Techno-economic survey of Organic Rankine Cycle (ORC) systems,' Renewable and Sustainable Energy Reviews, vol. 22, pp. 168-186, 2013.

S. Lecompte, H. Huisseune, M. Van Den Broek, B. Vanslambrouck, and M. De Paepe, 'Review of organic Rankine cycle (ORC) architectures for waste heat recovery,' Renewable and Sustainable Energy Reviews, vol. 47, pp. 448-461, 2015.

H. Nami, I. S. Ertesvag, R. Agromayor, L. Riboldi, and L. O. Nord, 'Gas turbine exhaust gas heat recovery by organic Rankine cycles (ORC) for offshore combined heat and power applications,' Energy, vol. 165, pp. 1060-1071, 2018.

F. Yang, H. Zhang, C. Bei, S. Song, and E. Wang, 'Parametric optimization and performance analysis of ORC for diesel engine waste heat recovery with a fin-and-tube evaporator,' Energy, vol. 91, pp. 128-141, 2015.

J. Bao and L. Zhao, 'A review of working fluid and expander selections for organic Rankine cycle,' Renewable and Sustainable Energy Reviews, vol. 24, pp. 325-342, 2013.

D. Connolly, H. Lund, B. V. Mathiesen, S. Werner, B. Moller, U. Persson, T. Boermans, D. Trier, P. A. Ostergaard, and S. Nielsen, 'Heat Roadmap Europe: Combining district heating with heat savings to decarbonise the EU energy system,' Energy Policy, vol. 65, pp. 475-489, 2014.

S. Maalouf, E. B. Ksayer, and D. Clodic, 'ORC finned-tube evaporator design and system performance optimization,' International Refrigeration and Air Conditioning Conference, Purdue University, 2012.

S. Hu, Z. Yang, J. Li, and Y. Duan, 'A review of multi-objective optimization in organic Rankine cycle (ORC) system design,' Energies, vol. 14, no. 20, 2021.

K. Deb, A. Pratap, S. Agarwal, and T. Meyarivan, 'A fast and elitist multiobjective genetic algorithm: NSGA-II,' IEEE Transactions on Evolutionary Computation, vol. 6, no. 2, pp. 182-197, 2002.

C. L. Hwang and K. Yoon, Multiple Attribute Decision Making: Methods and Applications. Berlin, Germany: Springer, 1981.

M. Behzadian, S. K. Otaghsara, M. Yazdani, and J. Ignatius, 'A state-of-the-art survey of TOPSIS applications,' Expert Systems with Applications, vol. 39, no. 17, pp. 13051-13069, 2012.

I. H. Bell, J. Wronski, S. Quoilin, and V. Lemort, 'Pure and pseudo-pure fluid thermophysical property evaluation and the open-source thermophysical property library CoolProp,' Industrial and Engineering Chemistry Research, vol. 53, no. 6, pp. 2498-2508, 2014.

C. E. Sprouse III and C. Depcik, 'Review of organic Rankine cycles for internal combustion engine exhaust waste heat recovery,' Applied Thermal Engineering, vol. 51, no. 1-2, pp. 711-722, 2013.

B. Saleh, G. Koglbauer, M. Wendland, and J. Fischer, 'Working fluids for low-temperature organic Rankine cycles,' Energy, vol. 32, no. 7, pp. 1210-1221, 2007.

A. E. Elahi, M. S. Islam, and S. Beg, 'Exergy analysis of organic Rankine cycle for waste heat recovery using low GWP refrigerants,' International Journal of Thermofluids, vol. 16, 2022.

H. D. Madhawa Hettiarachchi, M. Golubovic, W. M. Worek, and Y. Ikegami, 'Optimum design criteria for an organic Rankine cycle using low-temperature geothermal heat sources,' Energy, vol. 32, no. 9, pp. 1698-1706, 2007.

M. Imran, B. S. Park, H. J. Kim, D. H. Lee, M. Usman, and M. Heo, 'Thermo-economic optimization of regenerative Organic Rankine Cycle for waste heat recovery applications,' Energy Conversion and Management, vol. 87, pp. 107-118, 2014.

J. Wang, Z. Yan, M. Wang, M. Li, and Y. Dai, 'Multi-objective optimization of an organic Rankine cycle for low-grade waste heat recovery using evolutionary algorithm,' Energy Conversion and Management, vol. 71, pp. 146-158, 2013.

W. Zhang, F. Yang, H. Zhang, X. Ping, and D. Yan, 'Numerical analysis and optimization design of fin-and-tube evaporator in organic Rankine cycle system for diesel engine waste heat recovery,' International Journal of Heat and Mass Transfer, vol. 175, 2021.

UNEP, The Montreal Protocol on Substances that Deplete the Ozone Layer, United Nations Environment Programme, Nairobi, 2018.

G. Tchanche, G. Papadakis, G. Lambrinos, and A. Frangoudakis, 'Fluid selection for a low-temperature solar organic Rankine cycle,' Applied Thermal Engineering, vol. 29, no. 11-12, pp. 2468-2476, 2009.

E. H. Wang, H. G. Zhang, B. Y. Fan, M. G. Ouyang, Y. Zhao, and Q. H. Mu, 'Study of working fluid selection of organic Rankine cycle (ORC) for engine waste heat recovery,' Energy, vol. 36, no. 5, pp. 3406-3418, 2011.

M. Bahrami, C. Pourfayaz, and A. Kasaeian, 'Low global warming potential (GWP) working fluids (WFs) for Organic Rankine Cycle (ORC) applications: A review,' Energy Reports, vol. 8, pp. 2775-2800, 2022.

C.-C. Wang, K.-Y. Chi, and C.-J. Chang, 'Heat transfer and friction characteristics of plain fin-and-tube heat exchangers, part II: Correlation,' International Journal of Heat and Mass Transfer, vol. 43, no. 15, pp. 2693-2700, 2000.

T. E. Schmidt, 'Heat transfer calculations for extended surfaces,' Refrigerating Engineering, vol. 57, pp. 351-357, 1949.

F. P. Incropera, D. P. DeWitt, T. L. Bergman, and A. S. Lavine, Fundamentals of Heat and Mass Transfer, 7th ed. Hoboken, NJ: John Wiley and Sons, 2011.

P. Virtanen et al., 'SciPy 1.0: Fundamental algorithms for scientific computing in Python,' Nature Methods, vol. 17, pp. 261-272, 2020.

V. Gnielinski, 'New equations for heat and mass transfer in turbulent pipe and channel flow,' International Chemical Engineering, vol. 16, no. 2, pp. 359-368, 1976.

Z. Liu and R. H. S. Winterton, 'A general correlation for saturated and subcooled flow boiling in tubes and annuli based on a nucleate pool boiling equation,' International Journal of Heat and Mass Transfer, vol. 34, no. 11, pp. 2759-2766, 1991.

M. G. Cooper, 'Saturation nucleate pool boiling - a simple correlation,' IChemE Symposium Series, vol. 86, pp. 785-793, 1984.

R. Turton, R. C. Bailie, W. B. Whiting, and J. A. Shaeiwitz, Analysis, Synthesis, and Design of Chemical Processes, 3rd ed. Upper Saddle River, NJ: Prentice Hall, 2008.

A. Bejan, G. Tsatsaronis, and M. Moran, Thermal Design and Optimization. New York: John Wiley and Sons, 1996.

W. M. Kays and A. L. London, Compact Heat Exchangers, 3rd ed. Malabar, FL: Krieger Publishing, 1998.

E. W. Lemmon, M. L. Huber, and M. O. McLinden, NIST Standard Reference Database 23: Reference Fluid Thermodynamic and Transport Properties (REFPROP), Version 9.1, National Institute of Standards and Technology, 2013.

M. Chea and S. Elbel, 'Experimental quantification of air-side row-by-row heat transfer coefficients on fin-and-tube heat exchangers,' International Journal of Refrigeration, vol. 131, pp. 657-665, 2021.

F. Halici, I. Taymaz, and M. Gunduz, 'The effect of the number of tube rows on heat, mass and momentum transfer in flat-plate finned tube heat exchangers,' Energy, vol. 26, no. 11, pp. 963-972, 2001.

S. Markovic, B. Jacimovic, S. Genic, M. Mihailovic, U. Milovancevic, and M. Otovic, 'Air side pressure drop in plate finned tube heat exchangers,' International Journal of Refrigeration, vol. 99, pp. 24-34, 2019.

L. S. Tong and Y. S. Tang, Boiling Heat Transfer and Two-Phase Flow, 2nd ed. Washington, DC: Taylor & Francis, 1997.

Y. A. Cengel and M. A. Boles, Thermodynamics: An Engineering Approach, 8th ed. New York: McGraw-Hill Education, 2015.

R. K. Shah and D. P. Sekulic, Fundamentals of Heat Exchanger Design. Hoboken, NJ: John Wiley and Sons, 2003.

E. N. Sieder and G. E. Tate, 'Heat transfer and pressure drop of liquids in tubes,' Industrial and Engineering Chemistry, vol. 28, no. 12, pp. 1429-1435, 1936.

Eurostat, 'Electricity prices for household consumers - bi-annual data (nrg_pc_204),' H2 2025. [Online]. Available: https://ec.europa.eu/eurostat.

Association of Issuing Bodies (AIB), European Residual Mixes 2024, 2024. [Online]. Available: https://www.aib-net.org.

W. De Paepe, D. Tuyttens, and M. Mendoza, Project mGT Recuperator Optimization, I-MARO-041 Meta-heuristics for Energy Systems, University of Mons, 2025.

Energuide, 'What is the average electricity and gas consumption of a Belgian household?' 2024. [Online]. Available: https://www.energuide.be.

C. A. Coello Coello, 'Theoretical and numerical constraint-handling techniques used with evolutionary algorithms: a survey of the state of the art,' Computer Methods in Applied Mechanics and Engineering, vol. 191, no. 11-12, pp. 1245-1287, 2002.

D. Coppitters, P. Tsirikoglou, W. De Paepe, K. Kyprianidis, A. Kalfas, and F. Contino, “RHEIA: Robust design optimization of renewable Hydrogen and dErIved energy cArrier systems,” Journal of Open Source Software, vol. 7, no. 75, p. 4370, 2022, doi: 10.21105/joss.04370

Appendix

Appendix A Model Parameters, Correlations

This appendix gathers the fixed model parameters, geometric definitions, heat-transfer correlations, cost coefficients, and feasibility checks used by the ORC forward evaluator.

Appendix A.1 Exhaust-Gas Property Correlations

The exhaust gas is represented by polynomial property correlations evaluated at the local mean gas temperature.

$$\rho_g(T_g) = 1.14 \times 10^{-6} T_g^2 - 1.77 \times 10^{-3} T_g + 1.0614 \quad [\mathrm{kg/m^3}] \tag{A.1}$$

$$c_{p,g}(T_g) = 0.246 T_g + 1000.6 \quad [\mathrm{J/(kg \cdot K)}] \tag{A.2}$$

$$k_g(T_g) = 7.32 \times 10^{-5} T_g + 0.0233 \quad [\mathrm{W/(m \cdot K)}] \tag{A.3}$$

$$\mu_g(T_g) = 3.94 \times 10^{-8} T_g + 1.76 \times 10^{-5} \quad [\mathrm{Pa \cdot s}] \tag{A.4}$$

Appendix A.2 Finned-Tube Geometry

The staggered tube bank uses transverse pitch $S_t = S$ and longitudinal pitch $S_l = S \sin(60°)$. The total number of tubes is $N_t = N_p N_r$ and the collar diameter is $d_c = d_o + 2t$. The following expressions define the gas-passage and heat-transfer areas used in both preheater and evaporator calculations.

$$\sigma_g = \left(\frac{p - t_f}{p}\right)\left(\frac{S - d_o}{S}\right) \tag{A.5}$$

$$A_m = \left(\frac{S - d_o}{2}\right)(p - t_f) \tag{A.6}$$

$$A_w = \left[SS_l - \frac{\pi d_o^2}{4} + \frac{\pi d_o (p - t_f)}{2}\right] N_r \tag{A.7}$$

$$d_h = \frac{4A_m}{A_w / L_{\mathrm{flow}}}, \quad L_{\mathrm{flow}} = S_l N_r \tag{A.8}$$

$$A_{g,\mathrm{front}} = S(N_p + 0.5)L, \quad A_{g,\mathrm{flow}} = \sigma_g A_{g,\mathrm{front}} \tag{A.9}$$

$$A_{g,\mathrm{bare}} = N_t \pi d_o L \left(1 - \frac{t_f}{p}\right) \tag{A.10}$$

$$A_{g,\mathrm{fin}} = \frac{2L}{p}\left[S\left(N_p + 0.5\right)S_l N_r - \frac{N_t \pi d_o^2}{4}\right] \tag{A.11}$$

$$A_{g,\mathrm{total}} = A_{g,\mathrm{bare}} + A_{g,\mathrm{fin}} \tag{A.12}$$

Appendix A.3 Wang et al. Gas-Side Coefficient Expressions

The gas-side Colburn j factor and friction factor are defined in Chapter 3. The geometry-dependent coefficient groups used in those correlations are listed here to keep the main chapter readable.

$$a1 = -0.361 - 0.042\frac{Nr}{\ln(Re)} + 0.158\ln\left[Nr\left(\frac{p}{dc}\right)^{0.41}\right] \tag{A.13}$$

$$a2 = -1.224 - \frac{0.076\left(\frac{Sl}{dh}\right)^{1.42}}{\ln(Re)} \tag{A.14}$$

$$a3 = -0.083 + 0.058\frac{Nr}{\ln(Re)} \tag{A.15}$$

$$a4 = -5.735 + 1.21\ln\left(\frac{Re}{Nr}\right) \tag{A.16}$$

$$b1 = -0.764 + 0.739\left(\frac{S}{Sl}\right) + 0.177\left(\frac{p}{dc}\right) - \frac{0.00758}{Nr} \tag{A.17}$$

$$b2 = -15.689 + \frac{64.021}{\ln(Re)} \tag{A.18}$$

$$b3 = 1.696 - \frac{15.695}{\ln(Re)} \tag{A.19}$$

Appendix A.4 Annular Fin Efficiency and Row Weighting

The equivalent annular fin radius is calculated using Schmidt's approximation, and the fin efficiency is evaluated using the exact modified-Bessel-function expression. Row-wise gas-side heat-transfer multipliers account for wake development and row-to-row variation through the tube bank.

$$re = 1.27\left(\frac{S}{2}\right)\left[\left(\frac{Sl}{S}\right) - 0.3\right]^{\frac{1}{2}}, \quad ro = \frac{dc}{2} \tag{A.20}$$

$$m = \left[\frac{2hg}{kf\ tf}\right]^{\frac{1}{2}} \tag{A.21}$$

$$\eta f = \left\{\frac{2ro}{[m(re^2 - ro^2)]}\right\} \times \left\{\frac{[I1(mre)K1(mro) - K1(mre)I1(mro)]}{[I0(mro)K1(mre) + K0(mro)I1(mre)]}\right\} \tag{A.22}$$

$$\eta_o = \frac{\left(A_{gbare} + \eta_f A_{gfin}\right)}{A_{gtotal}} \tag{A.23}$$

$$hg,i = Fi\ hg \tag{A.24}$$

$$F_i = \frac{N_r R_i}{\sum_{k=1}^{N_r} R_k} \tag{A.25}$$

Table A.1. Row weighting factors for the gas-side heat-transfer multiplier.

Row factor	1	2	3	4	≥5
R_k	1.00	0.60	0.55	0.53	0.52

Appendix A.5 Preheater Effectiveness Relation

The preheater contains sensible heat transfer on both sides. The following finite-capacity-rate relation is used during the preheater length iteration, where the calculated heat duty is matched to the enthalpy-based preheating duty.

$$C_r = \frac{C_{\min}}{C_{\max}} \tag{A.26}$$

$$\varepsilon_p = 1 - \exp\left\{\frac{NTU^{0.22}}{C_r}[\exp(-C_r NTU^{0.78}) - 1]\right\} \tag{A.27}$$

Appendix A.6 Purchased-Equipment Cost Coefficients

Table A.2. Purchased-equipment cost correlation coefficients and material factors.

Component	Size parameter X	K_1	K_2	K_3	Fm	Unit of X
Evaporator	$A_{g,total}$	4.3247	−0.3030	0.1634	1.12	m²
Preheater	$A_{g,total}$	4.3247	−0.3030	0.1634	1.12	m²
Condenser	A_c	4.3247	−0.3030	0.1634	1.12	m²
Pump	P_p	3.3892	0.0536	0.1538	1.50	kW
Turbine	P_t	2.2476	1.4965	−0.1618	1.00	kW

Appendix B Full OAT Sensitivity Plots for Geometric Variables

The full geometric OAT plots are collected here because p, S, N_p, and N_r mainly affect cost and pressure-drop behaviour rather than the thermodynamic cycle states.

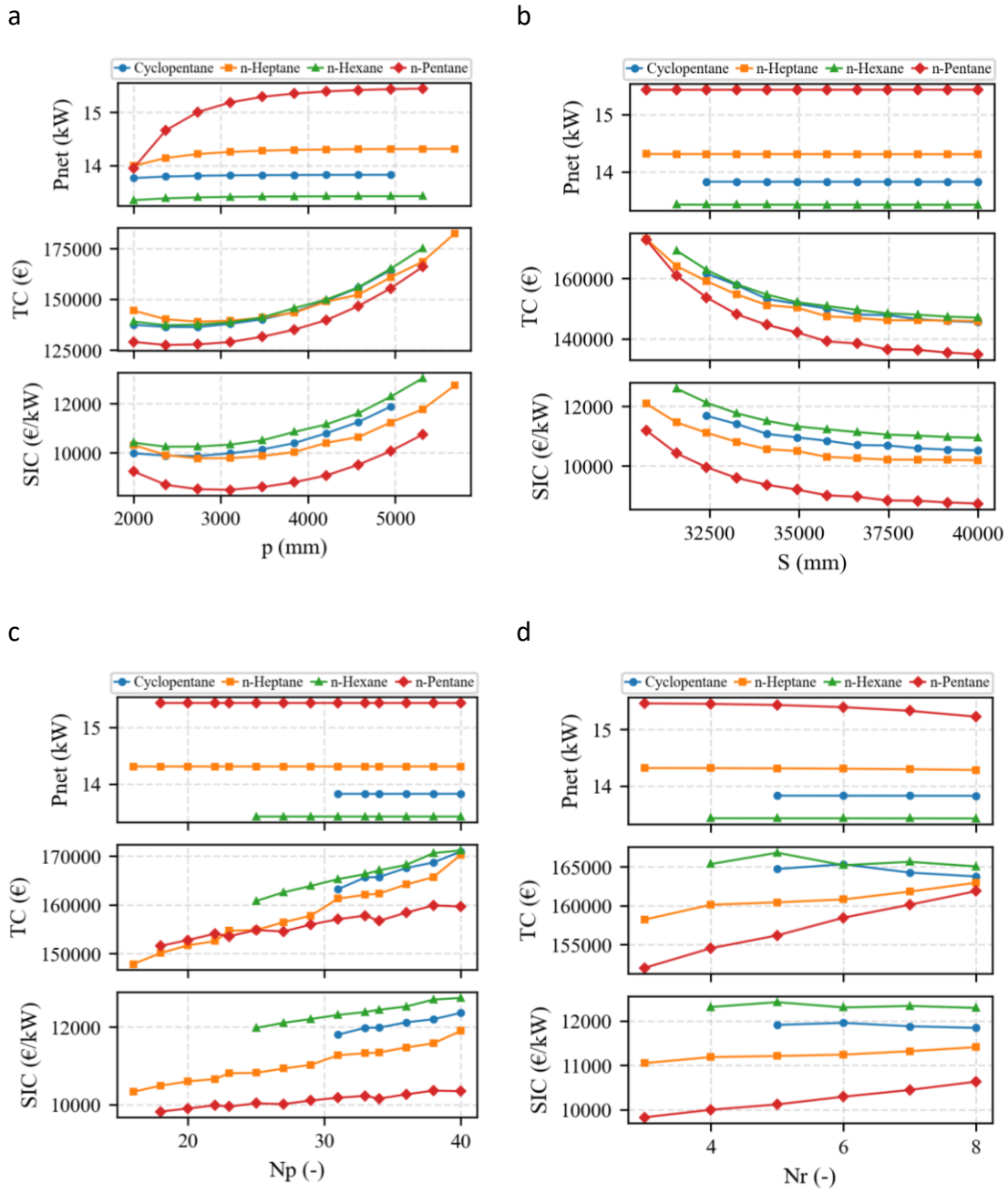

Figure B.1. OAT sensitivity of the geometric decision variables for the four selected hydrocarbons: (a) fin pitch p, (b) tube spacing S, (c) number of tubes per row N_p, and (d) number of tube rows N_r. For each variable, Pnet, TC, and SIC are shown while all other variables are fixed at their base-case values.

Appendix C Full Three-Dimensional Pareto Fronts

The three-dimensional Pareto fronts show the simultaneous trade-off among SIC, TED, and Pnet for each retained hydrocarbon. The red star marks the TOPSIS-selected best-compromise design within each fluid-specific Pareto set.

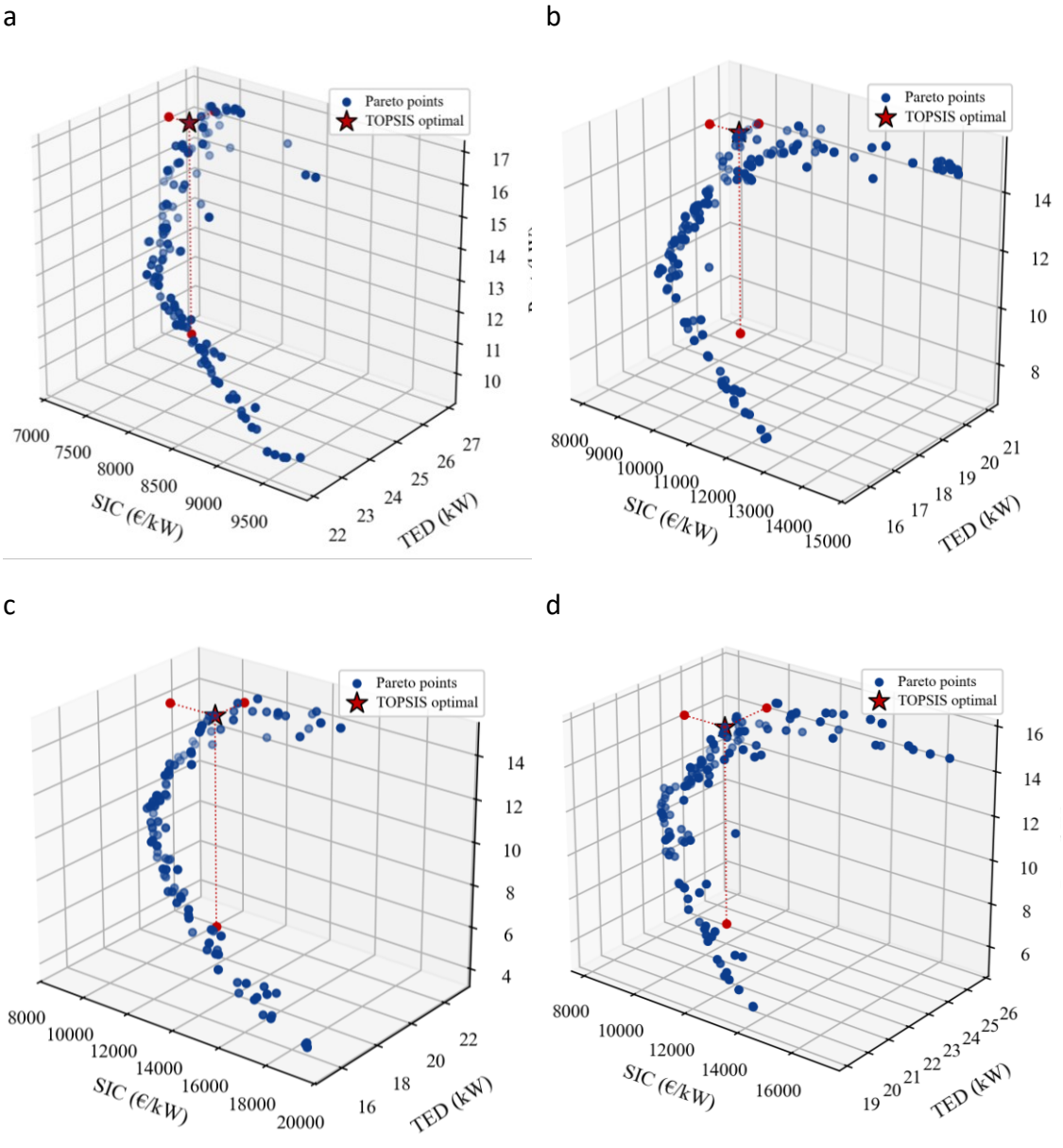

Figure C.1. Three-dimensional Pareto fronts for the four selected hydrocarbon working fluids: (a) n-pentane, (b) cyclopentane, (c) n-hexane, and (d) n-heptane. Each plot shows the trade-off between SIC, TED, and Pnet, with the TOPSIS-selected best-compromise point highlighted.

Appendix D: Python/RHEIA Implementation Notes

This appendix summarizes the Python/RHEIA implementation used to run the NSGA-II optimization. Only the essential implementation files and optimization settings are reported here; the complete scripts are provided electronically with the thesis.

D.1 Implementation files

The optimization workflow consists of the ORC evaluator, a RHEIA case-description file, a design-space file, and a run script. The ORC evaluator developed in Chapter 3 calculates the thermodynamic cycle, heat-exchanger performance, gas-side pressure-drop penalties, exergy destruction, and cost indicators. RHEIA calls this evaluator during the NSGA-II optimization.

Table D.1. Main implementation files.

File	**Purpose**
orc_model.py	ORC forward evaluator returning SIC, TED, and Pnet
case_description.py	Connects the ORC evaluator to the RHEIA case structure
design_space.csv	Defines lower and upper bounds of the seven decision variables
run_optimization.py	Launches the NSGA-II optimization
Post_Process.py	Removes penalty solutions, extracts Pareto fronts, applies TOPSIS, and saves plots

The RHEIA case-description file links the optimization framework to the ORC evaluator through a single import statement.

Listing D.1. RHEIA case-description interface.

```
from rheia.CASES.MGT_ORC.orc_model import evaluate
```

The evaluator receives the seven-variable design vector and returns the objective values used by NSGA-II. The full evaluator source code is not repeated in the thesis because the model equations and correlations are already documented in Chapter 3 and Appendix A.

D.2 NSGA-II optimization settings

The optimization was launched using the RHEIA optimization module. The initial population was generated automatically using Latin Hypercube Sampling, and the run was stopped after a fixed evaluation budget. The settings used in the run script are shown in Listing D.2.

Listing D.2. RHEIA NSGA-II optimisation setup.

```
import rheia.OPT.optimization as rheia_opt

dict_opt = {
    "case": "MGT_ORC",
    "objectives": {"DET": (-1, -1, 1)},
    "population size": 20,
    "stop": ("BUDGET", 800),
    "results dir": "results_1",
    "x0": ("AUTO", "LHS"),
    "cx prob": 0.9,
    "mut prob": 0.1,
    "eta": 0.2,
    "n jobs": 1
}

rheia_opt.run_opt(dict_opt)
```

The objective setting (-1, -1, 1) represents the three-objective formulation used in Chapter 4: SIC and TED are minimized, while Pnet is maximized. The population size is 20, and the total budget is 800 objective-function evaluations. A crossover probability of 0.9 and mutation probability of 0.1 are used. The complete optimization and post-processing scripts are retained as supplementary electronic files.